https://doi.org/10.5194/egusphere-2026-1730
Preprint. Discussion started: 4 May 2026

Impacts of aerosols on the tornado potential: A case study in Yangtze River Delta, China

Rumo Wang[1], Tianyi Fan[1], Zhanqing Li[2], and Jianping Guo[3]

[1]Faculty of Geographical Science, Beijing Normal University, Beijing, 100875, China
[2]Department of Atmospheric and Oceanic Science, Earth System Science Interdisciplinary Center, University of Maryland, USA
[3]State Key Laboratory of Severe Weather Meteorological Science and Technology & Specialized Meteorological Support Technology Research Center, Chinese Academy of Meteorological Sciences, Beijing, 100081, China

Correspondence: Tianyi Fan (fantianyi@bnu.edu.cn)

Abstract. Extensive observational and modeling studies have demonstrated that aerosols can modify extreme rainfall and convective storms. Their impacts on the genesis and development of tornadoes remain largely unexplored. By incorporating data assimilation into WRF-Chem simulations, we successfully simulate the whole life cycle of a supercell tornado and demonstrate the roles of anthropogenic aerosols. It is found that aerosols can enhance tornado potential, quantified here by the Significant Tornado Parameter, and affect storm motion, precipitation evolution, and cold-pool structure chiefly through two mechanisms. First, aerosols enhance condensational heating within the 0.3–1 km layer. Second, aerosols reduce near-surface evaporative cooling within the low-level updraft core by shifting it away from regions of strong rain evaporation. Together, these thermodynamic effects increase heating and thermal buoyancy, accelerating the low-level updraft. The aerosol-caused strengthening of the updraft enhances low-level convergence and deepens storm-relative inflow, leading to increased ingestion of streamwise vorticity in the 0–1 km layer, which dominates the enhancement of the tornado potential. This study gains new insights into the thermodynamic and dynamical pathways through which aerosols can influence extreme weather.

1 Introduction

Among the hazards generated by deep convection, tornadoes are particularly damaging, with near-surface wind speeds that can exceed 90 m s^{-1} (World Meteorological Organization, 2017), posing major threats to life and property (National Weather Service, 2024). Explicitly resolving tornado-scale vortex structure requires ultra-high-resolution simulations, typically using horizontal grid spacings of 50 m or less (Xue et al., 2014; Orf et al., 2017; Snook et al., 2019; Sun et al., 2019; Coffer et al., 2023; Kong et al., 2025). Such resolutions remain computationally prohibitive for operational forecasting and research applications. Consequently, tornado potential is often assessed using composite environmental parameters that combine key thermodynamic and dynamical ingredients relevant to tornadogenesis. These diagnostics provide practical guidance for identifying tornado-favorable environments and prioritizing forecasting attention (Litta et al., 2012; Taszarek et al., 2016; LeBel et al., 2021).

https://doi.org/10.5194/egusphere-2026-1730
Preprint. Discussion started: 4 May 2026

Tornado-potential diagnostics are subject to substantial uncertainty in operational forecasting (Brotzge et al., 2013). These uncertainties arise from large-scale circulation variability (Barrett and Gensini, 2013; Lepore et al., 2017; Tippett, 2018; Tippett et al., 2022), as well as land-surface heterogeneity and surface roughness (Kellner and Niyogi, 2014; Frazier et al., 2019; Markert et al., 2019; Fan et al., 2023; Li et al., 2024). In contrast, the potential influence of aerosols on tornadoes has rarely been investigated. Previous numerical studies have shown that smoke aerosols can modify cloud properties and radiative heating, enhancing vertical wind shear near the surface, therefore increasing tornado potential (Saide et al., 2015, 2016). These studies primarily emphasized aerosol-induced radiative effects and changes in cloud lifetime. However, a large body of research indicates that aerosols can also invigorate convection by increasing the microphysical heating, a process that is central to tornadogenesis (Khain et al., 2005; Jiang et al., 2018; Li et al., 2019a; Chen et al., 2020; Marinescu et al., 2021; Igel and van den Heever, 2021).

According to cold- and mixed-phase invigoration theory (Andreae et al., 2004; Rosenfeld et al., 2008), aerosols reduce precipitation efficiency in the warm-cloud layer, enabling more liquid condensate to be transported upward and enhancing ice-phase latent heating aloft, thereby strengthening deep convection. This mechanism is supported by the observational evidence of Li et al. (2011). Warm-phase invigoration theory (Wang, 2005; Fan et al., 2007, 2018) further proposes that, under sufficiently high supersaturation, enhanced condensation within warm clouds can directly accelerate updrafts. Whether aerosols can systematically enhance latent heating and updraft strength at low levels above cloud base remains actively debated (Grabowski and Morrison, 2020; Fan and Khain, 2021; Igel and van den Heever, 2021; Romps et al., 2023; Varble et al., 2023; Öktem et al., 2023; Fan et al., 2025). Regardless of the theoretical framework, the response of low-level updrafts to aerosol perturbations warrants further investigation, as low-level updraft strength is a critical constraint on tornado potential, particularly for supercell tornadoes.

An intensified low-level updraft can enhance storm-relative inflow (Coffer et al., 2023), promoting the import of streamwise horizontal vorticity into the storm (Davies-Jones, 1984; Dahl et al., 2014; Coffer et al., 2020; Goldacker and Parker, 2023; Peters et al., 2023) and further supporting the near-surface tornadic vortex. Numerous studies have shown that tornadic environments are characterized by stronger near-surface dynamical support for streamwise vorticity ingestion than nontornadic environments (Thompson et al., 2003; Craven and Brooks, 2004; Coffer et al., 2019; LeBel et al., 2021; Zhang et al., 2025). These results indicate that the low-level updraft is a key factor governing tornado-favorable conditions. However, whether aerosols can enhance low-level condensational heating and, in turn, strengthen low-level updrafts and tornado potential in real tornado cases remains largely untested.

In addition to their influence on updrafts, aerosols can modify precipitation intensity and spatial distribution by invigorating convection (Xiao et al., 2016; Li et al., 2019b; Cao et al., 2021; Feng et al., 2023; Yun et al., 2024), thereby affecting evaporative cooling and the subsequent cold-pool response (Kalina et al., 2014; Kawecki et al., 2016). Excessively strong or rapidly advancing cold pools can undercut and suppress updrafts, disrupting vorticity ingestion and inhibiting tornadogenesis (Markowski et al., 2002; Grzych et al., 2007; Lerach et al., 2008; Lebo and Morrison, 2014; Markowski and Richardson, 2014; Zheng and Chen, 2014; Guarriello et al., 2018; Fischer and Dahl, 2020; Wu et al., 2022). Idealized simulations have shown that aerosol-induced changes in cold-pool–updraft configuration can influence tornado-like vortices (Lerach et al., 2008; Ler-

https://doi.org/10.5194/egusphere-2026-1730
Preprint. Discussion started: 4 May 2026

ach and Cotton, 2012), but this mechanism has not been verified in real tornado cases nor directly compared with aerosol impacts mediated through condensational heating.

Although aerosol invigoration effects on tornadoes are conceptually plausible, several challenges hinder their evaluation. First, high-resolution observations of key near-surface processes remain extremely difficult to obtain (Tanamachi et al., 2013; Fischer et al., 2024), and observational data alone are often insufficient to isolate aerosol effects from meteorological co-variability (Stevens and Feingold, 2009; Grabowski, 2018; Varble et al., 2023; Fan et al., 2025). This limitation motivates simulation-based studies that provide access to otherwise unobservable variables and allow controlled aerosol perturbation experiments. Second, simulations of organized deep convection are highly sensitive to initial conditions and therefore exhibit limited predictability (Zhang et al., 2003; Hohenegger and Schär, 2007; Zhuang et al., 2020; Wang et al., 2024), making data assimilation essential for improving realism (Sun et al., 2022; Yang et al., 2025). Third, potential-temperature tendencies in the Weather Research and Forecasting (WRF) model do not close numerically with diagnosed heating rates from individual model processes, complicating thermodynamic attribution and necessitating a closure-consistent diagnostic framework.

In this study, we examine how aerosols influence tornado potential by modifying the thermodynamic and dynamical environment of a real EF3 supercell tornado. We employ the WRF model coupled with Chemistry (WRF-Chem) integrated with a hybrid assimilation framework to realistically reproduce the storm's thermodynamic and dynamical structure. Sensitivity experiments with and without anthropogenic emissions are conducted to isolate aerosol effects on tornado-favorable conditions. To attribute mechanisms rigorously, we apply a source-ingredient decomposition of the vertical-momentum budget and construct a numerically closed budget for heating rates using the WRFlux framework. The remainder of this paper is organized as follows: Section 2 describes the case, model configuration, experimental design and the main analysis methods; Section 3 presents the main results; and Section 4 provides a summary and discussion.

2 Methods

2.1 Case Description

This study examines an EF3 supercell tornado that occurred in Shengze in the Yangtze River Delta (YRD), China, on 14 May 2021 (Wu et al., 2022; Yuan et al., 2024). The YRD is a highly urbanized and industrialized region characterized by substantial anthropogenic aerosol emissions. On the synoptic scale, the environment was favorable for severe convection and tornadogenesis, featuring (i) very cold upper-tropospheric temperatures accompanied by divergence aloft near 200 hPa, (ii) positive vorticity advection downstream of a mid-level trough at 500 hPa, and (iii) a persistent southwesterly low-level jet at 850 hPa that transported moisture and supported atmospheric instability (see Fig. S1 in the Supplement).

The 0.5° elevation-angle reflectivity observations show the evolution of the supercell as it propagated southeastward from 18:05 to 18:50 local standard time (LST; UTC+8), merging with smaller convective cells along its path (Fig. 1a–d). This storm coincided with a pronounced strengthening of the low-level inbound-outbound radial velocity couplet (Fig. 1e and f), indicating enhanced near-surface rotation and increasingly favorable conditions for tornadogenesis. Radar observations at

https://doi.org/10.5194/egusphere-2026-1730
Preprint. Discussion started: 4 May 2026

18:56 LST (Fig. 1d and f) show a classic supercell structure associated with the tornado, which occurred between 18:50 and 19:12 LST near Shengze.

2.2 Model configuration and experimental design

2.2.1 WRF-Chem ensemble simulations

This study employed WRF-Chem version 4.2.2, a chemistry-enabled configuration of the WRF modeling system, to perform the model experiments (Grell et al., 2005). WRF-Chem incorporates online coupling between aerosol processes and meteorological fields, enabling feedbacks associated with aerosol radiative effects and aerosol–cloud interactions (Chapman et al., 2009).

Aerosol impacts were examined by conducting a pair of sensitivity experiments. Both simulations shared the same basic model configuration and emission inventories (Table S1), but differed only in whether anthropogenic emissions were enabled (ALL run) or disabled (NoAero run). Cloud droplet number concentrations were updated consistently with aerosol loading in each experiment. The anthropogenic aerosol effect (hereafter referred to as the Aero effect) was quantified as the difference between the ALL and NoAero simulations, encompassing aerosol impacts on radiation, cloud microphysics, and thermodynamics.

The model configuration comprised two nested domains (Fig. 2a), with horizontal resolutions of 9 km for d01 and 3 km for d02. All simulations were initialized at 08:00 LST on 13 May 2021. An ensemble of 80 members was generated using the random control-variable perturbation option of the WRF Data Assimilation (WRFDA) system. Each member was integrated forward through a 28-hour spin-up period, followed by a 5-hour data-assimilation period and a 3-hour analysis period used for evaluation. From the full ensemble, 70 members exhibiting the best agreement with observations were selected for analysis. Unless otherwise stated, results presented in Section 3 represent ensemble means computed from these 70 members.

https://doi.org/10.5194/egusphere-2026-1730
Preprint. Discussion started: 4 May 2026

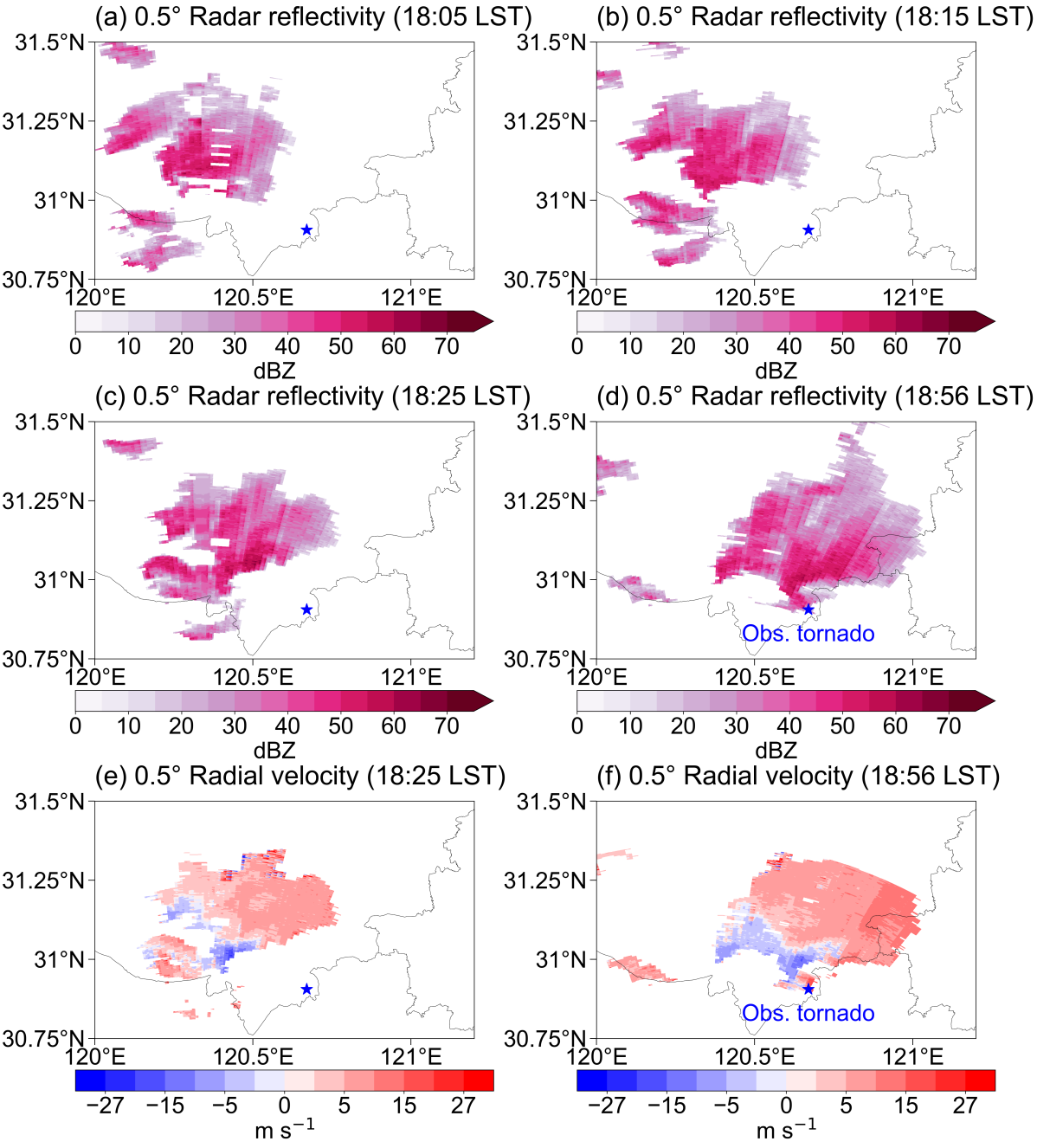

Figure 1. Radar reflectivity (shaded; units: dBZ) at (a) 18:05, (b) 18:15, (c) 18:25, (d) 18:56 LST, and radial velocity (shaded; units: m s^{-1}) at (e) 18:25 and (f) 18:56 LST at Hangzhou station (30.22° N, 120.15° E) scanned at a 0.5° elevation angle. The blue stars indicate the observed tornado position, and the label "Obs. tornado" appears only in panels (d) and (f), during the tornado lifetime (18:50–19:12 LST).

https://doi.org/10.5194/egusphere-2026-1730
Preprint. Discussion started: 4 May 2026

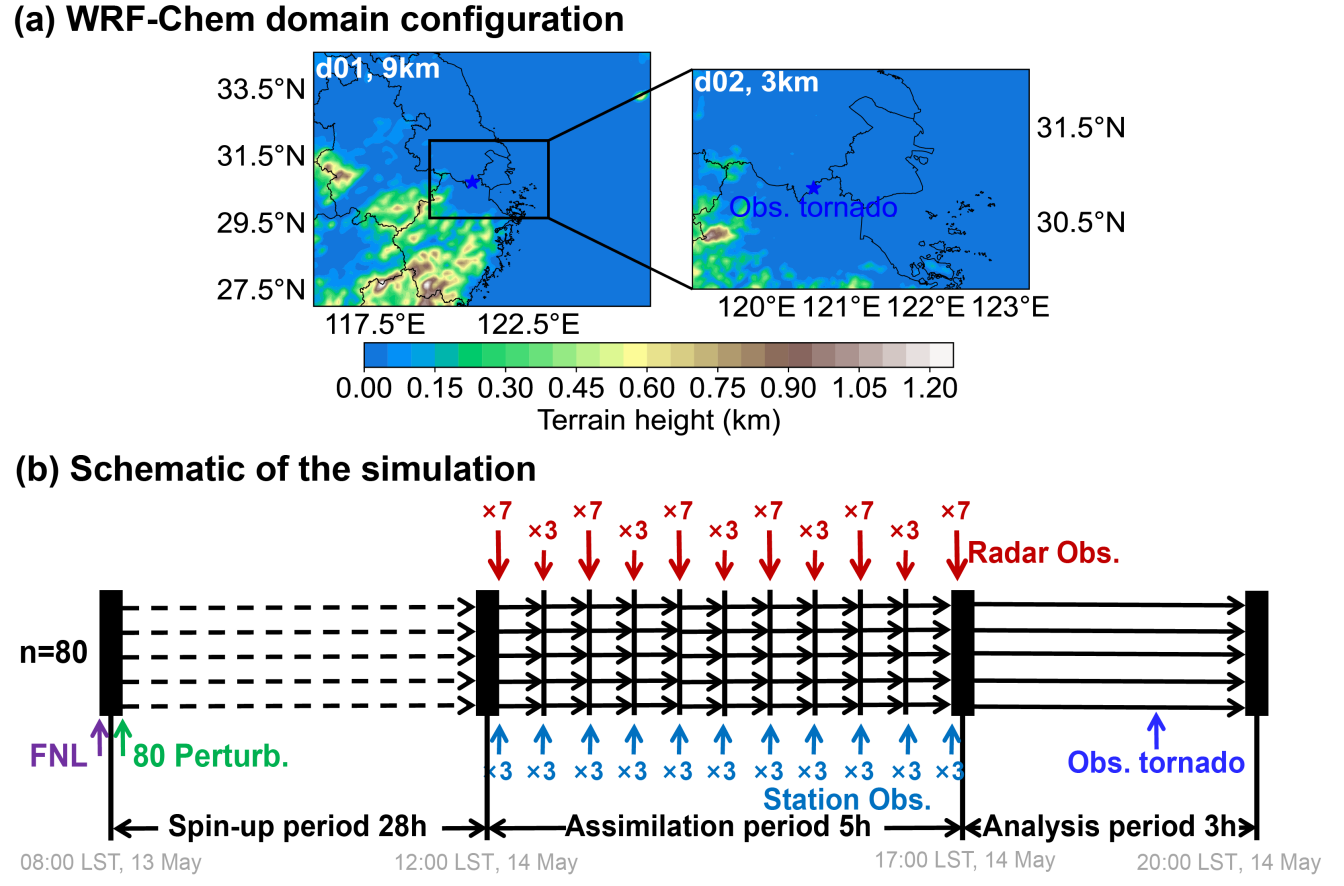

Figure 2. (a) WRF-Chem model domain configuration with terrain height (shading). The left panel presents the parent domain (d01), and the black rectangles indicate the extent of the nested domain (d02), which is shown in detail in the right panel. The horizontal resolutions of d01 and d02 are 9 and 3 km, respectively. The blue stars indicate the observed tornado position. (b) Schematic of the WRF-Chem ensemble simulation. The model is initialized and forced with NCEP FNL reanalysis data. The ensemble consists of 80 members, each starting from a distinct random CV-perturbed initial field derived from the FNL reanalysis data. The simulation includes three stages: a 28 h spin-up period (from 08:00 LST 13 May to 12:00 LST 14 May 2021), a 5 h assimilation period (from 12:00 LST 14 May to 17:00 LST 14 May), and a 3 h analysis period (from 17:00 LST 14 May to 20:00 LST 14 May 2021). During the assimilation period, two types of observations (i.e., single-polarization Doppler radar data and surface automatic weather station data) are assimilated every 30 min. At each full-hour assimilation time (e.g., 12:00, 13:00 LST), radar observations are repeatedly assimilated seven times, and at each off-hour assimilation time (e.g., 12:30, 13:30 LST) they are assimilated three times, whereas surface station data are assimilated three times at every assimilation time.

https://doi.org/10.5194/egusphere-2026-1730
Preprint. Discussion started: 4 May 2026

2.2.2 Hybrid data assimilation in the WRFDA system

During the data-assimilation period, surface observations from automatic weather stations (AWS), including near-surface wind speed, wind direction, temperature, humidity, and pressure, were assimilated together with S-band Doppler radar observations from the Hangzhou and Qingpu sites. Assimilation was performed every 30 minutes using a cycling framework (Fig. 2b) within the WRFDA hybrid ensemble–variational framework (Buehner, 2005; Wang et al., 2007), which combines three-dimensional variational assimilation (3D-Var; Sasaki, 1958) with the ensemble transform Kalman filter (ETKF; Evensen, 1994).

The background-error covariance consisted of 20% static covariance and 80% ensemble-based flow-dependent covariance. At each assimilation time, observations were assimilated sequentially through multiple analysis updates, with the analysis from each update serving as the background for the next. Radar observations were assimilated seven times at full-hour cycles and three times at half-hour cycles, while AWS observations were assimilated three times at each cycle. This configuration was selected based on sensitivity tests demonstrating reduced root-mean-square errors in near-surface wind fields and improved representation of precipitation and hydrometeor distributions.

AWS observations were quality-controlled following the QX/T 118-2020 standard (China Meteorological Administration, 2020), supplemented by an empirical orthogonal function-based method (Shang et al., 2024). Radar observations were quality-controlled using a fuzzy-logic algorithm (Berenguer et al., 2006; Radhakrishna et al., 2019). Only quality-controlled observations were assimilated. Identical data-assimilation configurations were applied in both the ALL and NoAero simulations, ensuring that differences between experiments arise solely from aerosol perturbations.

2.3 Diagnostics for the tornado potential

Although multiple formulations of STP exist (Thompson et al., 2003, 2012; Zhang et al., 2025), tornado-favorable environments were quantified using the Significant Tornado Parameter (STP; Eq. 1) following Thompson et al. (2003). A detailed justification for this choice is provided in Appendix A.

$$\mathrm{STP} = \frac{\mathrm{SRH1}}{100\,m^2\,s^{-2}} \cdot \frac{\mathrm{SHR6}}{20\,m\,s^{-1}} \cdot \frac{2000 - \mathrm{MLLCL}}{1500\,m} \cdot \frac{\mathrm{MLCAPE}}{1000\,J\,kg^{-1}} \tag{1}$$

Here, SRH1 denotes storm-relative helicity integrated over the 0–1 km above ground level (AGL) layer, and SHR6 represents the 0–6 km AGL bulk wind shear magnitude. MLLCL and MLCAPE are calculated from the lowest 100 hPa mixed-layer parcel, representing its lifting condensation level and convective available potential energy, respectively. STP is calculated by multiplying these four normalized terms, the dynamical components related to SRH1 and SHR6, and the thermodynamic components related to MLLCL and MLCAPE. When STP exceeds 1, it is more favorable for tornadogenesis and therefore indicates enhanced tornado potential.

SRH1 is obtained by vertically integrating the local storm-relative helicity ($\mathrm{SRH_{local}}$) at each layer within 0–1 km,

$$\mathrm{SRH1} = \int_{z=0\,\mathrm{km}}^{z=1\,\mathrm{km}} \mathrm{SRH_{local}}\,\mathrm{d}z \tag{2a}$$

https://doi.org/10.5194/egusphere-2026-1730
Preprint. Discussion started: 4 May 2026

where

$$\mathrm{SRH}_{\mathrm{local}} = |\mathbf{V}_H - \mathbf{C}| \cdot |\boldsymbol{\omega}_H| \cdot \cos\alpha \tag{2b}$$

where $|\boldsymbol{\omega}_H|$ represents the horizontal-vorticity magnitude, $|\mathbf{V}_H - \mathbf{C}|$ denotes the storm-relative inflow speed, and α is the angle between $\boldsymbol{\omega}_H$ and $\mathbf{V}_H - \mathbf{C}$. The terms $\mathbf{V}_H$ and $\mathbf{C}$ denote the horizontal wind vector and storm-motion vector, respectively. Following the default implementation (Maddox, 1976), $\mathbf{C}$ is assigned a magnitude equal to 75% of the 3–10 km AGL layer-mean wind speed, with its direction displaced 30° clockwise from the corresponding layer-mean wind vector. Larger SRH1 indicates greater streamwise vorticity available for ingestion through the storm-relative inflow, which supports low-level updraft rotation and enhances tornado potential.

Larger SHR6 indicates strong deep-layer shear which promotes organized storm structure and a persistent rotating updraft, thus supporting supercell development and maintenance (Thompson et al., 2003; Craven and Brooks, 2004). MLLCL provides an estimate of the convective cloud-base height. It also reflects the near-surface moisture environment, which is important for subcloud evaporation and cold-pool thermodynamics that are relevant to tornadogenesis (Markowski et al., 2002; Thompson et al., 2003; Craven and Brooks, 2004; Fischer and Dahl, 2020).

Prior studies found that the SRH1 term is more sensitive for separating tornadic from nontornadic environments, whereas the role of MLLCL term is secondary (Thompson et al., 2003; Craven and Brooks, 2004; Coffer et al., 2019; LeBel et al., 2021). By contrast, SHR6 and MLCAPE typically constrain the precondition of whether storms can organize and persist with sustained rotating updrafts. However, they typically provide weaker skill in directly discriminating tornado intensity. Instead, they primarily act as the thresholds that support storm organization and the tornado potential (Craven and Brooks, 2004; Grams et al., 2012).

2.4 Tracking study areas

To focus on storm-relevant regions, STP areas and updraft cores are dynamically tracked at each 10-minute model output time using a seeded region-growing (SRG) algorithm consisting of four steps (Adams and Bischof, 1994). First, an initial search window and seed point were specified. Second, at subsequent times, the search window was advected eastward based on the previous seed-point motion to maintain temporal continuity, and a new seed point was identified within the updated window. Third, the SRG algorithm was applied, expanding outward from the seed point using a percentile-based threshold computed within the current search window. This adaptive thresholding approach avoids reliance on fixed thresholds and accommodates temporal variability. Fourth, steps two and three were repeated at each time step.

The initial search window spanned 30°–32° N and 119.5°–122° E. The seed point was defined as the grid cell with the maximum STP value within the window, subject to the condition that radar reflectivity exceeded 30 dBZ within a one-grid-cell buffer to ensure inclusion of the hook-echo region. The growth threshold was set to the 75th percentile of STP values greater than one within the search window.

In addition, low-level updraft cores within the 0–1 km layer were tracked to examine how aerosol perturbations modify convergence and inflow near regions of enhanced tornado potential. The initial search window was defined as the STP area

https://doi.org/10.5194/egusphere-2026-1730
Preprint. Discussion started: 4 May 2026

expanded by a three-grid-cell buffer to account for modest spatial offsets between convergence and updraft maxima. The seed point was identified as the local maximum 0–1 km updraft within this window, and the growth threshold was defined as the 90th percentile of updraft values within the window.

2.5 Vertical momentum budget

To quantify any processes contributing to aerosol-induced updraft changes, a vertical momentum budget was constructed following Jeevanjee and Romps (2015) and Abulikemu et al. (2016, 2019). Eq. (3) decomposes the total vertical acceleration ($\frac{\mathrm{D}w}{\mathrm{D}t}$, denoted a_{Total}) into (i) a thermodynamically driven term, buoyant acceleration, denoted a_B, and (ii) a dynamically driven term, the vertical acceleration produced by the vertical perturbation pressure-gradient force (VPPGF), denoted a_{VPPGF}.

$$\frac{\mathrm{D}w}{\mathrm{D}t} = a_B + a_{\mathrm{VPPGF}} \tag{3}$$

In Eq. (4), buoyant acceleration (a_B) is decomposed into thermal buoyant acceleration ($a_{B(\mathrm{TH})}$), water-vapor buoyant acceleration ($a_{B(\mathrm{WV})}$), and condensate loading acceleration ($a_{B(\mathrm{CL})}$).

$$a_B = a_{B(\mathrm{TH})} + a_{B(\mathrm{WV})} + a_{B(\mathrm{CL})} \tag{4}$$

In most cases, thermal buoyant acceleration $a_{B(\mathrm{TH})}$ dominates the a_B, $a_{B(\mathrm{TH})} = g\theta'/\theta_0$ where g is the acceleration due to gravity, θ' is the perturbation potential temperature, and θ_0 is the base-state potential temperature. $a_{B(\mathrm{WV})} = g\,r'_v\,((1-\varepsilon))/\varepsilon$ where r'_v is the water-vapor mixing ratio and ε is the dry-air to water-vapor gas-constant ratio. $a_{B(\mathrm{CL})} = -g\,r_c$, where r_c is the total condensate mixing ratio.

The a_{VPPGF} term in Eq. (3) is decomposed into five components associated with distinct physical processes (Eq. 5),

$$\begin{aligned} a_{\mathrm{VPPGF}} &= a_{B\text{-VPPGF}} + a_{\mathrm{Extension}} + a_{\mathrm{Curvature}} + a_{\mathrm{Twisting}} + a_{\mathrm{Density}} \\ &= -\frac{1}{\rho_0}\frac{\partial p^*_{B\text{-VPPGF}}}{\partial z} - \frac{1}{\rho_0}\frac{\partial p^*_{\mathrm{Extension}}}{\partial z} - \frac{1}{\rho_0}\frac{\partial p^*_{\mathrm{Curvature}}}{\partial z} - \frac{1}{\rho_0}\frac{\partial p^*_{\mathrm{Twisting}}}{\partial z} - \frac{1}{\rho_0}\frac{\partial p^*_{\mathrm{Density}}}{\partial z} \end{aligned} \tag{5}$$

where ρ_0 denotes the base-state density. Here, $a_{B\text{-VPPGF}}$, $a_{\mathrm{Extension}}$, $a_{\mathrm{Curvature}}$, a_{Twisting}, and a_{Density} are accelerations associated with the buoyancy-induced VPPGF, fluid-extension, horizontal-curvature, vertical-twisting, and vertical-velocity–density, respectively. Their corresponding partial pressure perturbations (i.e., $p^*_{B\text{-VPPGF}}$, $p^*_{\mathrm{Extension}}$, $p^*_{\mathrm{Curvature}}$, p^*_{Twisting}, and p^*_{Density}) can be obtained by solving the Poisson equations in Eqs. (6a–6e):

$$-\nabla^2 p^*_{B\text{-VPPGF}} = -\frac{\partial(\rho_0 B)}{\partial z} \tag{6a}$$

$$-\nabla^2 p^*_{\mathrm{Extension}} = \rho_0\left(\frac{\partial^2 u}{\partial x^2} + \frac{\partial^2 v}{\partial y^2} + \frac{\partial^2 w}{\partial z^2}\right) \tag{6b}$$

$$-\nabla^2 p^*_{\mathrm{Curvature}} = 2\rho_0\left(\frac{\partial v}{\partial x}\frac{\partial u}{\partial y}\right) \tag{6c}$$

https://doi.org/10.5194/egusphere-2026-1730
Preprint. Discussion started: 4 May 2026

$$-\nabla^2 p^*_{\text{Twisting}} = 2\rho_0 \left(\frac{\partial u}{\partial z}\frac{\partial w}{\partial x} + \frac{\partial v}{\partial z}\frac{\partial w}{\partial y} \right) \tag{6d}$$

$$-\nabla^2 p^*_{\text{Density}} = -\rho_0 \frac{\mathrm{d}^2 \ln \rho_0}{\mathrm{d}z^2} w^2 \tag{6e}$$

where B is buoyancy, and (u, v, w) are the corresponding wind components. The buoyancy-induced VPPGF term is interpreted as a dynamically induced compensation to buoyancy-driven ascent, acting to offset the tendency toward unrealistically large local divergence (i.e., the "vacuum formation") as parcels accelerate upward.

The Poisson equation is solved numerically using a finite-difference solver. Homogeneous Dirichlet conditions ($p^* = 0$) are applied at all boundaries, consistent with previous studies where this choice is regarded as appropriate and unambiguous (Jeevanjee and Romps, 2015; Abulikemu et al., 2016). All calculations are conducted at the model output time interval with no additional temporal interpolation.

2.6 WRFlux

We diagnosed a numerically closed potential-temperature (θ) budget from the WRF-Chem output using WRFlux v1.2.0 (Göbel, 2021). With our WRF configuration, the θ tendencies are diagnosed as the sum of microphysical, advection, SGS turbulent diffusion, LW radiative and SW radiative heating rates, which reproduces the model θ tendency over each averaging interval. We use 10-s-averaged heating rates diagnosed by WRFlux to better approximate instantaneous heating rates in WRF-Chem. WRFlux does not separate individual microphysical subprocesses (e.g., condensation, evaporation, deposition) heating rates. We therefore used the WRF-Chem archived microphysical subprocess tendencies and rescaled them so that their sum matches the WRFlux-diagnosed total microphysical heating rate.

3 Results

3.1 Model evaluation

Because cold-pool structure and near-surface thermodynamic conditions play critical roles in shaping tornado-favorable environments, we first evaluate the simulated precipitation and surface temperature against ground-based meteorological station observations. Our simulation reproduces the evolution of rainfall adequately well, although the precipitation intensity is overestimated (Fig. 3a). The spatial distribution of accumulated precipitation between 17:00 and 19:00 LST is captured reasonably well, with the simulated precipitation center closely matching observations, despite an overestimation of the areal extent (Fig. 3b).

The simulated 2-m temperature field at 19:00 LST exhibits a low-temperature center over the Taihu Lake (Fig. 3c), consistent with observations and collocated with the precipitation maximum and associated cold pool. However, due to the overestimated

https://doi.org/10.5194/egusphere-2026-1730
Preprint. Discussion started: 4 May 2026

precipitation, simulated temperatures within the cold pool are lower than observed. Simulated near-surface $PM_{2.5}$ concentrations are compared with air-quality monitoring data in Fig. 3d. The model generally underestimates pollutant concentrations, likely due to uncertainties in emissions, limited spatial resolution, and biases in boundary-layer and convection parameterizations that promote excessive mixing. As a result, aerosol impacts diagnosed in this study likely represent a conservative estimate of the true anthropogenic aerosol influence.

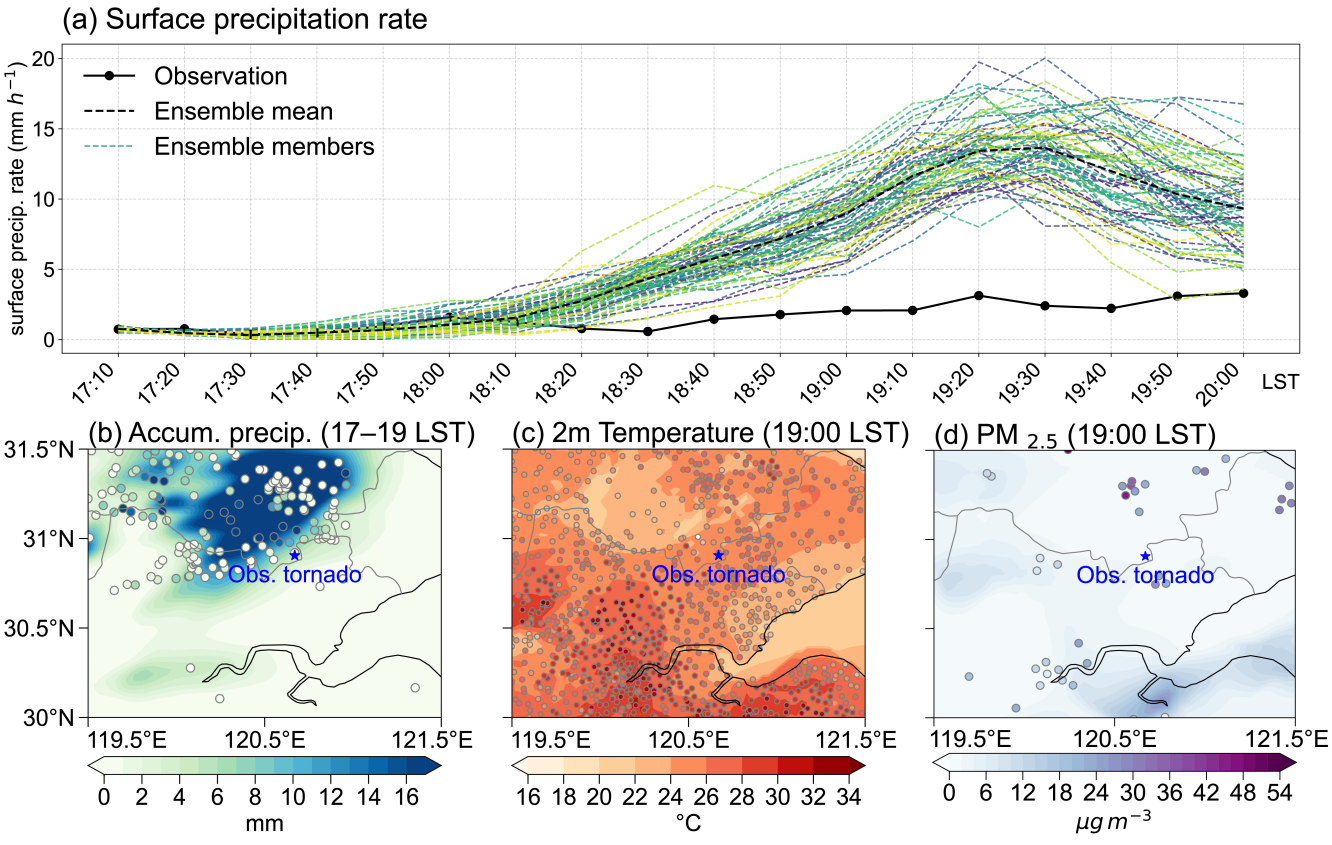

Figure 3. (a) Temporal evolution of near-surface precipitation rate (units: mm h^{-1}) from observations (black solid line) averaged over stations and the ensemble mean (black dashed line), and ensemble members (colored dashed lines) of the ALL run simulation averaged over model grid points corresponding to the station locations. Spatial distributions of (b) accumulated precipitation (shaded; units: mm) between 17:00 and 19:00 LST, (c) 2 m temperature (shaded; units: °C) at 19:00 LST, and (d) mass concentration of $PM_{2.5}$ (shaded; units: μg m^{-3}) at 19:00 LST from observations (circles) and the ensemble mean of the ALL run (shaded). The blue stars in (b)–(d) denote the observed tornado position.

3.2 Aerosol effects on STP

The spatiotemporal evolution of STP from 17:20 to 20:00 LST is shown in Fig. 4 for the ALL simulation. Regions of persistently high STP exist south of the tornado location, largely driven by the SRH1 component. However, these regions are not

https://doi.org/10.5194/egusphere-2026-1730
Preprint. Discussion started: 4 May 2026

directly relevant to tornado potential until the mesoscale convective system propagates southeastward from the northwest and intersects the high-STP environment, as indicated by radar reflectivity exceeding 35 dBZ. This storm motion is well reproduced by the model and aligns with radar observations (Fig. 1). The STP study area within the storm-influenced region is tracked following the procedure described in Section 2.4. The location of the tornado is well embedded within the tracked STP area during the tornadogenesis period near 19:00 LST.

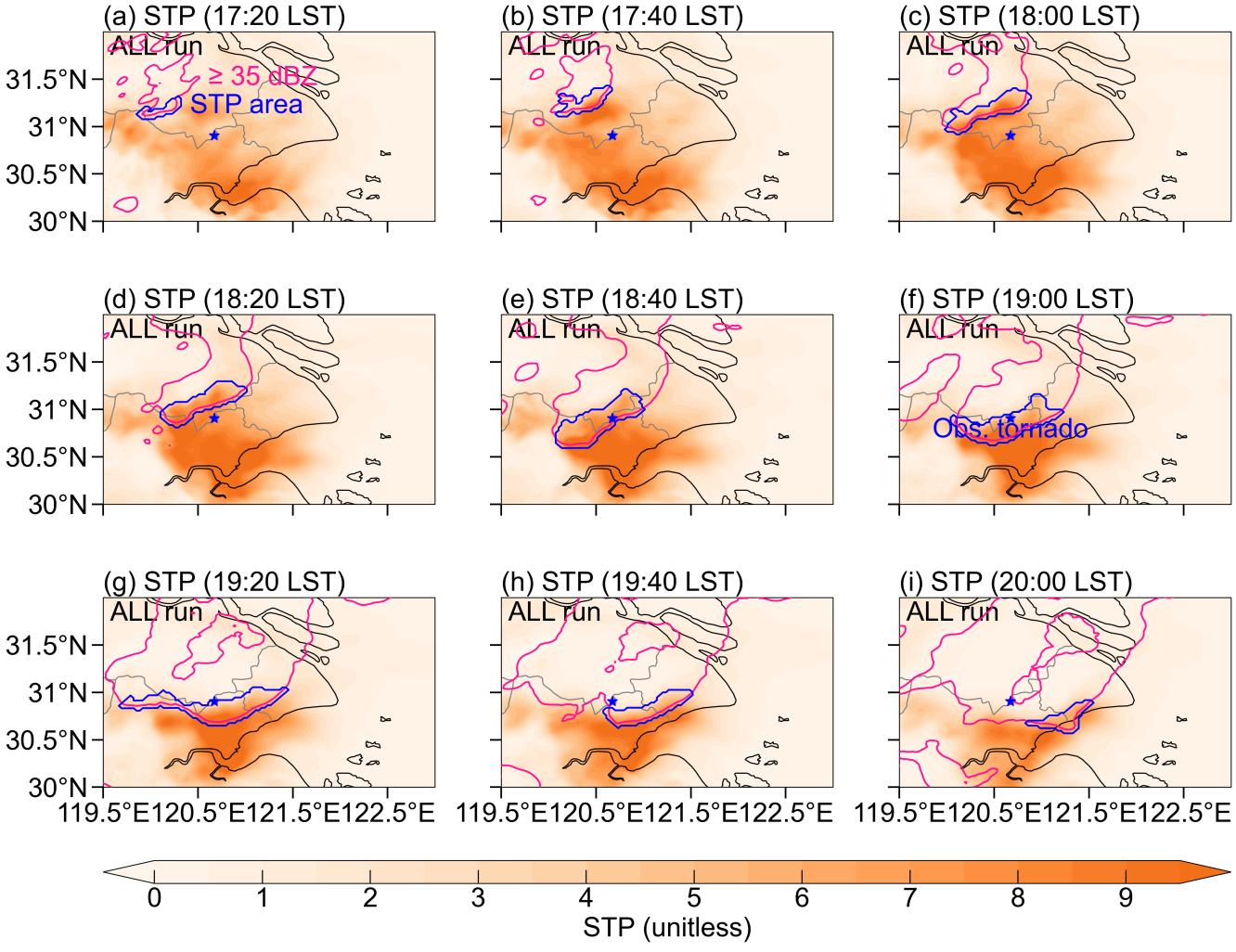

Figure 4. STP (shaded; unitless) at twenty-minute intervals from 17:20 LST to 20:00 LST from the ALL run simulation. The rose-red contours indicate areas with radar maximum reflectivity over 35 dBZ. The blue contours indicate the tracked STP study area, with blue stars indicating the location of the observed tornado, which lasted from 18:50 to 19:12 LST. The label "Obs. tornado" appears only in panel (f), during the tornado lifetime (18:50–19:12 LST).

https://doi.org/10.5194/egusphere-2026-1730
Preprint. Discussion started: 4 May 2026

Figure 5 shows the time evolution of STP and its components averaged over the tracked STP area for both the ALL and NoAero simulations. In both experiments, STP exceeds unity and increases sharply prior to 17:50 LST, indicating increasingly favorable conditions for tornadogenesis regardless of aerosol loading. After 17:50 LST, the ensemble-mean STP in the ALL simulation remains elevated, whereas STP in the NoAero simulation exhibits a modest decline. Following the midpoint of the observed tornado life cycle at 19:00 LST, STP gradually decreases but remains above one.

From 18:10 LST on, STP in ALL run is larger than that in NoAero run, indicating that the tornado potential is enhanced by the aerosol effects. SRH1 term contributes most to the total STP and drives the STP increase, much larger than the thermodynamic terms of MLLCL and MLCAPE do. This suggests that the low-level dynamical condition (SRH1) contributes more than the thermodynamic ones (MLLCL and MLCAPE) to tornado potential in this case. Similar results are obtained using other tornado potential diagnostics, supporting the robustness of this result (Appendix A). During 18:30–19:10 LST, the Wilcoxon signed-rank test applied to the 70 paired ensemble-member differences indicates statistically significant aerosol-induced changes in both STP and SRH1. This test is more appropriate than the paired t-test because it does not assume normally distributed samples. For the following analysis, 19:00 LST is tracked as the time unless indicated otherwise.

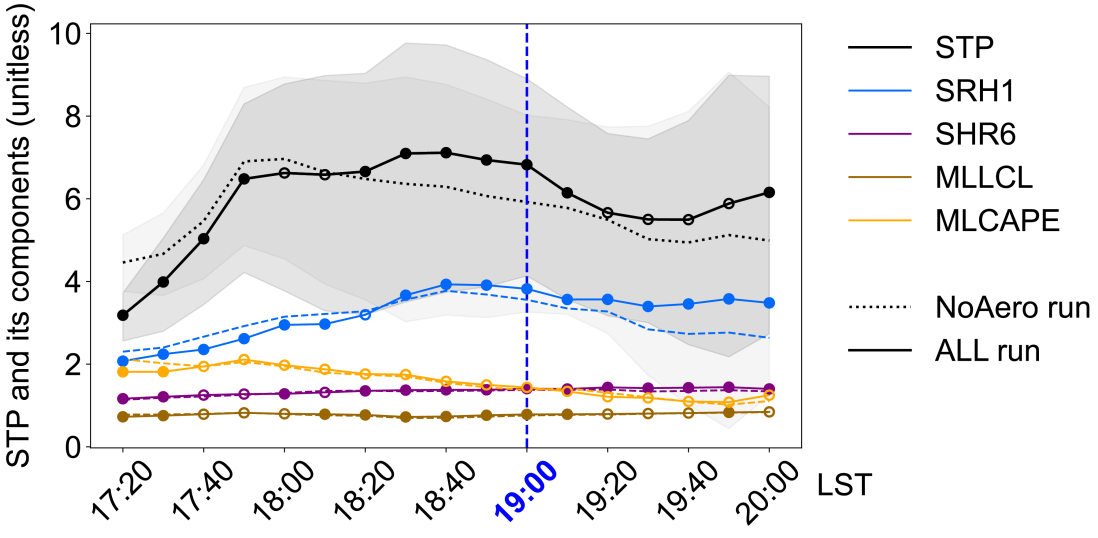

Figure 5. Time evolution of STP and its components (unitless) averaged over the STP area. The black lines represent STP, and the colored lines denote the SRH1 term (sky blue), SHR6 term (purple), MLLCL term (brown), and MLCAPE term (orange). The solid lines represent the ALL run and the dashed lines represent those from the NoAero run. The shading denotes the interquartile range of STP of ensemble members in the ALL run (dark gray) and the NoAero run (light gray). The blue dashed vertical line represents the temporal midpoint of the observed tornado life cycle (19:00 LST), which hereafter serves as the analysis time. Filled and open circles along the solid lines denote significant and nonsignificant differences, respectively, based on the 0.05 significance level.

The cause of SRH1 enhancement is further investigated by decomposing the local storm-relative helicity ($\mathrm{SRH}_{\mathrm{local}}$, the vertical decomposition of SRH1, see Eq. 2a and 2b) into the storm-relative inflow, the horizontal vorticity, and the cosine

https://doi.org/10.5194/egusphere-2026-1730
Preprint. Discussion started: 4 May 2026

of their included angle ($\cos\alpha$) terms. At 19:00 LST, aerosols predominantly enhanced $\mathrm{SRH_{local}}$ at most grid points, while only a minority of grid points exhibited a reduction in $\mathrm{SRH_{local}}$ (Fig. S2). We analyzed both the grid points where $\mathrm{SRH_{local}}$ increased (Fig. 6a) and where $\mathrm{SRH_{local}}$ decreased (Fig. 6b) by aerosol effects. The increase in $\mathrm{SRH_{local}}$ is found to be driven primarily by enhanced storm-relative inflow (Fig. 6c). Horizontal vorticity and $\cos\alpha$ terms are the principal contributors to the reduction of $\mathrm{SRH_{local}}$ (Fig. 6d). These findings suggest that the overall increase in SRH1 (0–1 km) is predominantly driven by aerosol-enhanced storm-relative inflow.

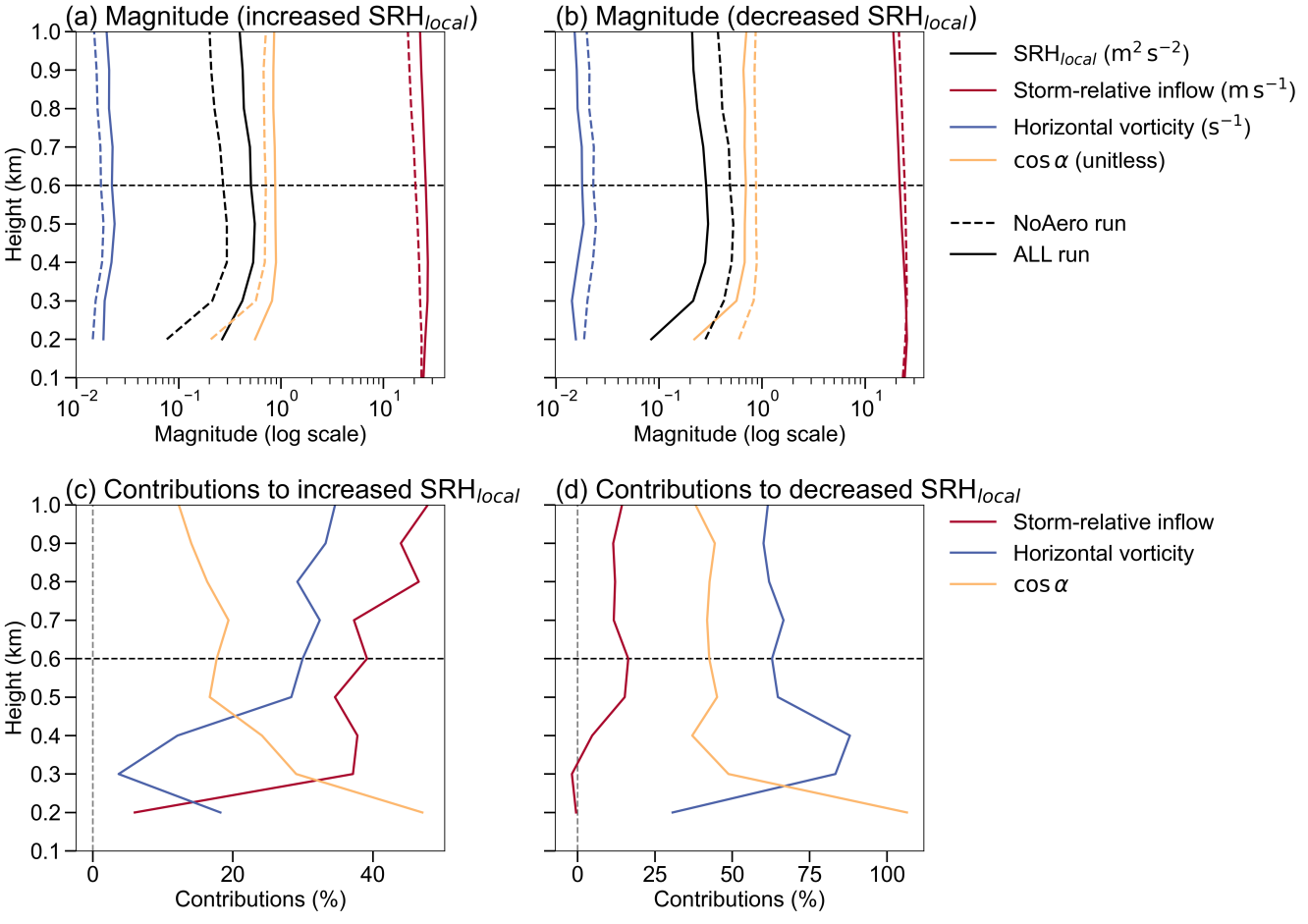

Figure 6. (a) Vertical profiles of the magnitudes of $\mathrm{SRH_{local}}$ (black lines; units: m s^{-2}) and its components, i.e., storm-relative inflow (red lines; units: m s^{-1}), horizontal vorticity (blue lines; units: s^{-1}), and $\cos\alpha$ (orange lines; unitless) at 19:00 LST averaged over grid points where aerosols enhance $\mathrm{SRH_{local}}$, which is the majority case. (b) Same as (a) but averaged over grid points where aerosols reduce $\mathrm{SRH_{local}}$, which is the minority case. (c) Vertical profiles of the contribution ratios of the components averaged over grid points where aerosols enhance $\mathrm{SRH_{local}}$. (d) Same as (c) but averaged over grid points where aerosols reduce $\mathrm{SRH_{local}}$. The horizontal dashed lines denote 0.6 km as a representative level for the diagnostics in Section 3.3 and Fig. 7.

https://doi.org/10.5194/egusphere-2026-1730
Preprint. Discussion started: 4 May 2026

3.3 Mechanisms of aerosol effects on tornado potential

3.3.1 Aerosol-induced enhancement of the storm-relative inflow

Figure 7a illustrates aerosol-induced changes in storm-relative inflow at the 0.6 km level, which is selected as a representative level within the 0–1 km layer because similar responses are found above and below this height. Regions of enhanced inflow coincide with the tracked STP area and are the focus of subsequent analysis. Decomposition of storm-relative inflow reveals that aerosols increase the horizontal wind speed and induce a counterclockwise turning of the wind direction, while exerting minimal influence on storm motion (Fig. 7b). These combined effects enhance storm-relative inflow.

To examine the three-dimensional wind response, we analyze low-level divergence and the locations of 0–1 km updraft cores (Figs. 7c–e). Within the STP area, southeasterly flow converges toward the updraft cores, and both convergence strength and updraft intensity are enhanced by aerosols. Regions of enhanced convergence align closely with regions of increased storm-relative inflow, indicating that aerosol-induced strengthening of convergence plays a central role.

Vertical momentum budget analysis indicates that enhanced convergence is not the primary driver of updraft intensification (Fig. S4c). Instead, aerosols first enhance the updraft through thermodynamic processes, which subsequently intensify low-level convergence and storm-relative inflow.

3.3.2 Aerosol effects on the low-level updraft

We focus on aerosol-induced changes in low-level updrafts. Figures 8a and 8b show the tracked 0–1 km updraft cores in the NoAero and ALL simulations, respectively. In the absence of aerosols, updraft cores are broader and more diffuse, whereas more concentrated and intense updraft cores are found in ALL simulations.

Figures 8c and 8d present the height–time evolution of aerosol-induced changes in updraft velocity and vertical acceleration, showing negative anomalies prior to 18:50 LST, followed by a sharp transition to positive anomalies as tornado potential is enhanced. Within the 0.3–1 km layer, increases in total vertical acceleration are dominated by a_B (Fig. 8e). Below 0.3 km, a_{VPPGF} is the dominant contributor (Fig. 8f).

Decomposition of a_B indicates that $a_{B(\mathrm{TH})}$ is the primary contributor to the aerosol-induced increase (Fig. S3). Further decomposition of the a_{VPPGF} shows that its aerosol-induced enhancement is largely attributable to the $a_{B\text{-}\mathrm{VPPGF}}$, with other dynamical contributions playing a negligible role (Fig. S4). The $a_{B\text{-}\mathrm{VPPGF}}$ term represents a dynamical adjustment that partially offsets a_B to maintain pressure balance in rising air parcels. Although this adjustment opposes a_B, its magnitude is smaller above 0.3 km, allowing thermodynamic forcing to dominate the net updraft response.

https://doi.org/10.5194/egusphere-2026-1730
Preprint. Discussion started: 4 May 2026

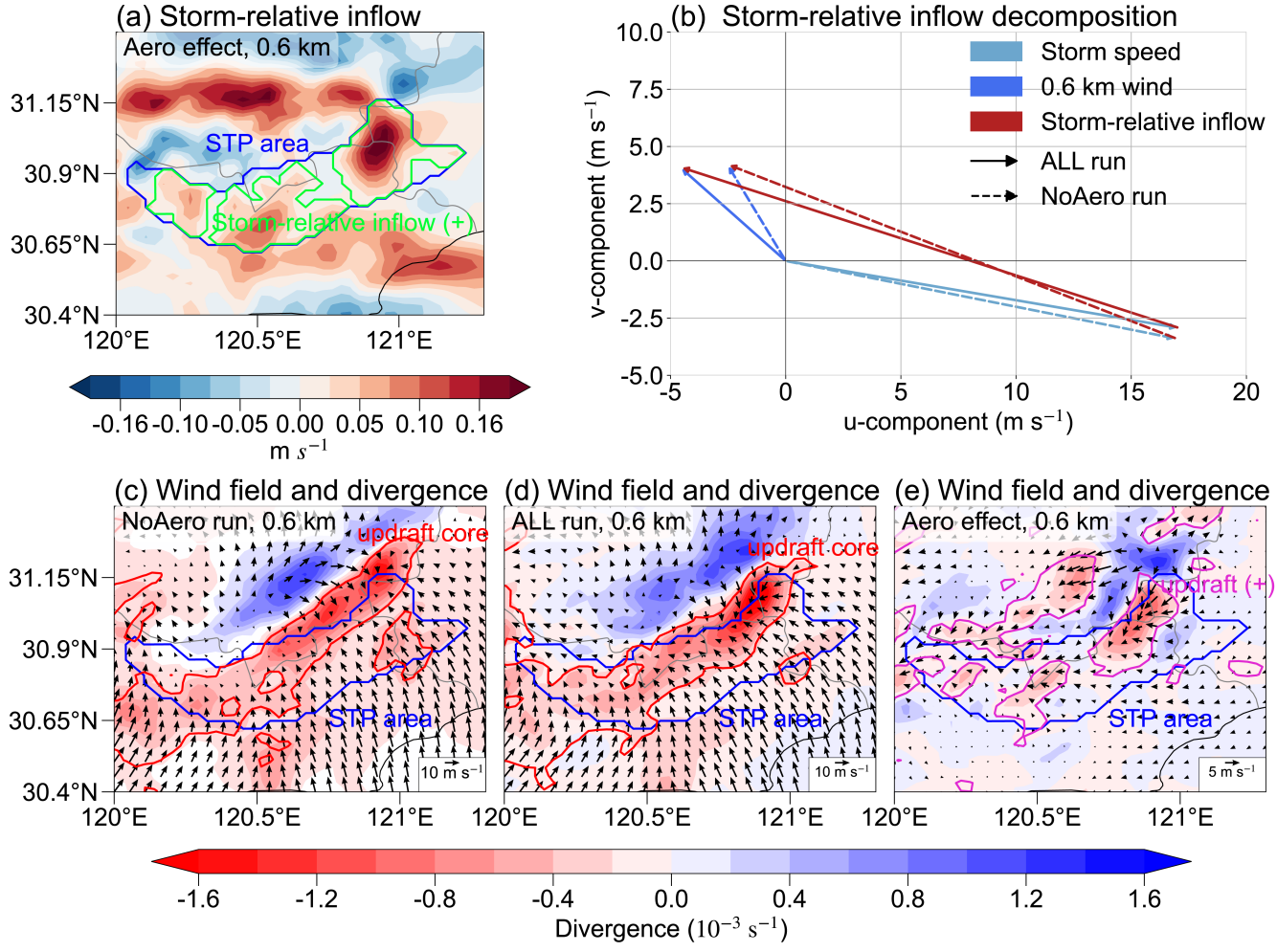

Figure 7. (a) Distribution of variations in storm-relative inflow (units: m s^{-1}) due to the aerosol effect. (b) Variations in storm-relative inflow (red arrows; units: m s^{-1}) and its components, i.e., horizontal wind at 0.6 km (blue arrows; units: m s^{-1}) and storm speed (light blue arrows; units: m s^{-1}), averaged over the tracked STP area from the NoAero (dashed vectors) and ALL (solid vectors) runs. Distribution of divergence (shaded; units: 10^{-3} s^{-1}) and wind field (arrows; units: m s^{-1}) from (c) NoAero run, (d) ALL run, and variations due to (e) the aerosol effect. The blue contours in (a), (c)–(e) represent the tracked STP area. The green contours in (a) represent the region where aerosols enhance the storm-relative flow. In (c)–(d), the blue contours indicate the tracked STP area, while the red contours represent 0–1 km updraft cores. The rose-red contour in (e) represents the 0–1 km updraft core enhanced by aerosols. All panels show data at 0.6 km at 19:00 LST.

https://doi.org/10.5194/egusphere-2026-1730
Preprint. Discussion started: 4 May 2026

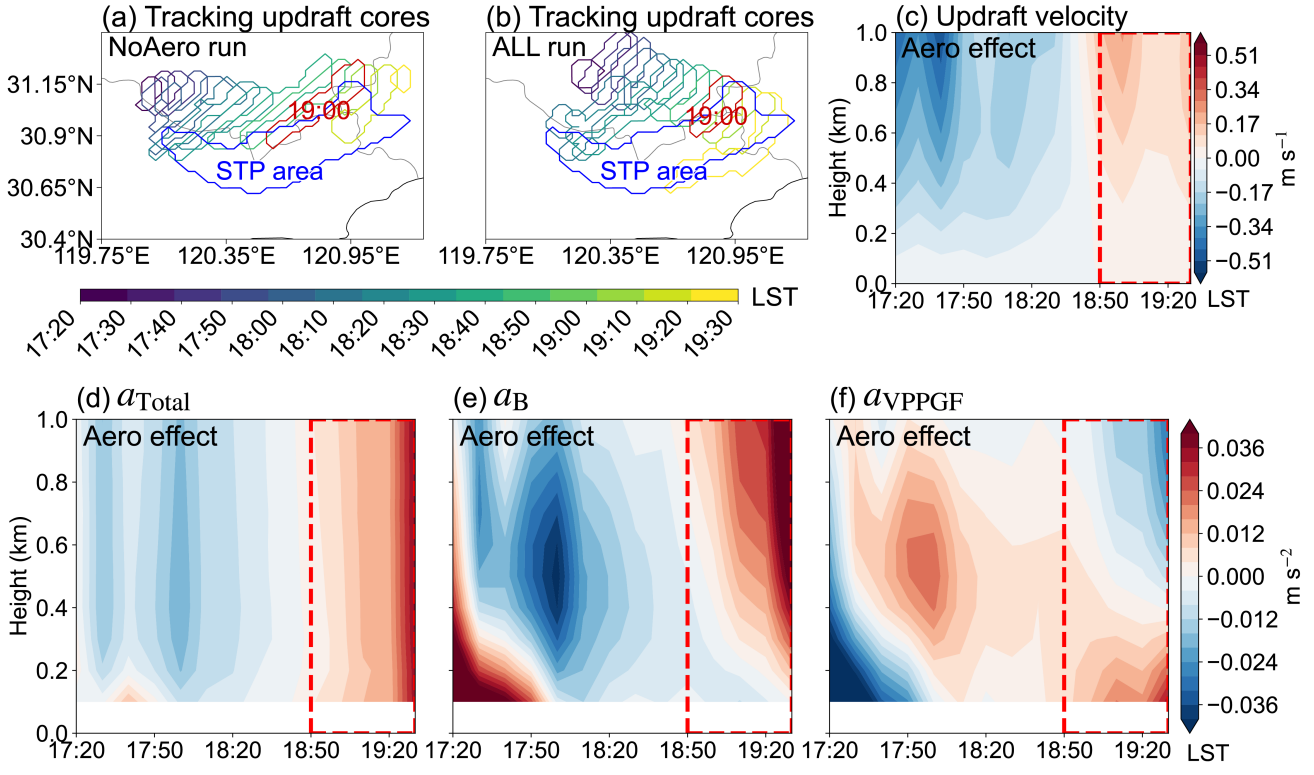

Figure 8. Tracked 0–1 km updraft cores at 10-minute intervals from 17:20 LST to 20:00 LST (colored contours) from (a) NoAero and (b) ALL runs. In (a)–(b), 19:00 LST is highlighted by red contours and the tracked STP areas are indicated by blue contours. Time–height cross-sections of variations in (c) updraft velocity (units: m s^{-1}), (d) vertical acceleration (a_{Total}; units: m s^{-2}), (e) buoyant acceleration (a_B; units: m s^{-2}), and (f) VPPGF-induced acceleration (a_{VPPGF}; units: m s^{-2}) due to aerosol effects. In (c)–(f), the red dashed rectangles highlight the focus window from 18:50 to 19:30 LST.

3.3.3 Aerosol effects on the buoyancy

To elucidate the thermodynamic mechanisms underlying enhanced buoyancy, we examine heating-rate diagnostics derived from WRFlux. At 19:00 LST, aerosols induce net atmospheric heating within the 0–1 km updraft cores, driven primarily by enhanced microphysical heating and partially offset by advective cooling (Fig. 9a). Radiative and turbulent diffusion contributions are comparatively small. The increase in microphysically-induced heating is primarily due to enhanced cloud water condensation and reduced rain evaporation (Fig. 9b). Enhanced condensational heating prevails above approximately 0.3 km, whereas below this level the suppression of evaporative cooling becomes increasingly important.

https://doi.org/10.5194/egusphere-2026-1730
Preprint. Discussion started: 4 May 2026

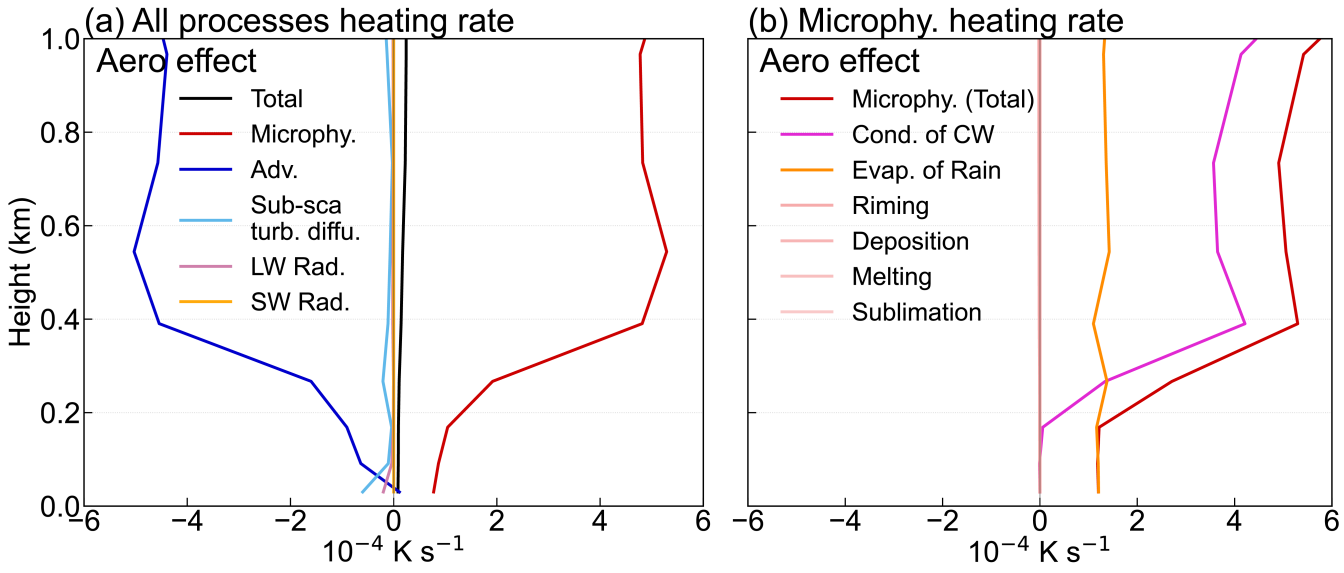

Figure 9. (a) Vertical profiles of the variations in total heating rate (Total; black) and contributions from each process, i.e., microphysical processes (Microphy.; red), advection (Adv.; blue), subgrid-scale turbulent diffusion (Sub-sca. turb. Diffu.; light blue), longwave radiation (LW Rad.; purple), and shortwave radiation (SW Rad.; light orange) due to the aerosol effect. (b) Vertical profiles of the variations in heating rates of microphysical processes (Microphy.; red) and contributions from individual sub-processes, i.e., condensation of cloud water (Cond. of CW; rose red), evaporation of rain (Evap. of Rain; orange), riming (light pink), deposition (light pink), melting (light pink), and sublimation (light pink) due to the aerosol effect. All heating rates are averaged over the tracked 0–1 km updraft cores at 19:00 LST, in units of 10^{-4} K s^{-1}.

While aerosol-driven enhancement of condensational latent heating is well known (Fan et al., 2018; Marinescu et al., 2021; Cao et al., 2021), the mechanism by which they reduce the low-level evaporative cooling requires further investigation. Aerosols cause the low-level updraft core to become more concentrated and displaced away from regions of strongest rain evaporation (Fig. 10). This spatial separation arises from an increased distance between the updraft core and primary precipitation regions. As a result, the updraft experiences weaker evaporative cooling and reduced cold-pool interference, allowing the convective system to remain sustained.

https://doi.org/10.5194/egusphere-2026-1730
Preprint. Discussion started: 4 May 2026

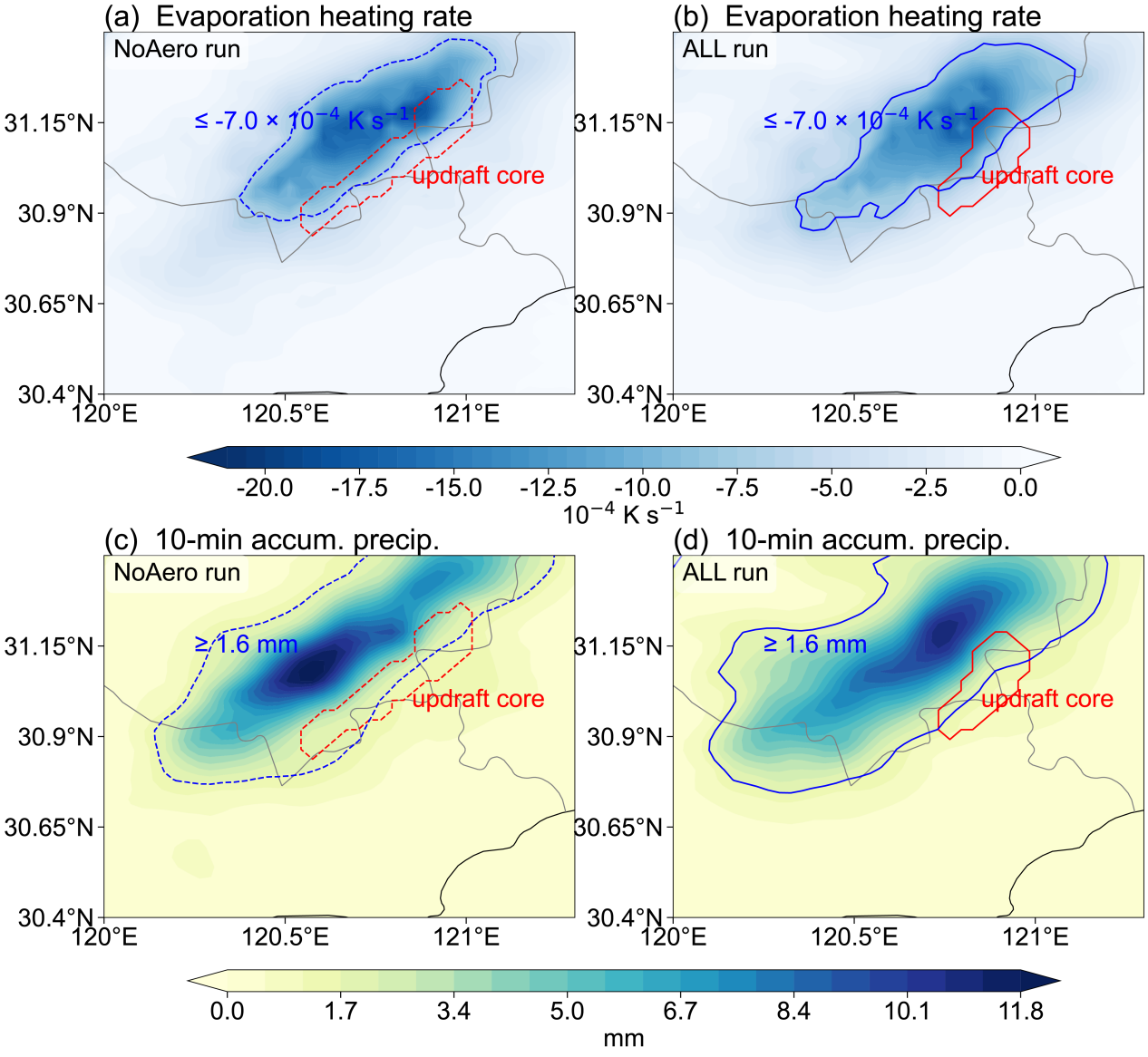

Figure 10. Variations in (a)–(b) heating rate of rain evaporation (shaded; units: 10^{-4} K s^{-1}) at 19:00 LST and (c)–(d) 10-minute accumulated precipitation (shaded; units: mm) near the surface due to the aerosol effect from 18:50 to 19:00 LST. The red contours represent 0–1 km updraft cores. The blue contours represent an evaporation heating rate of -7.0×10^{-4} K s^{-1} in (a)–(b) or 10-minute accumulated precipitation of 1.6 mm in (c)–(d). Dashed contours are from the NoAero run and solid contours are from the ALL run.

3.4 New mechanisms and implications for the aerosol condensational invigoration

The above analyses led us to propose a new mechanism that may provide a new pathway for the aerosol condensational invigoration. Aerosols enhance tornado potential primarily through dynamical effects associated with increased SRH1, which

https://doi.org/10.5194/egusphere-2026-1730
Preprint. Discussion started: 4 May 2026

plays the dominant role in the aerosol-induced enhancement in STP. The increase in SRH1 arises mainly from strengthened storm-relative inflow, rather than changes in horizontal vorticity or thermodynamic instability.

The enhanced storm-relative inflow is linked to aerosol-induced strengthening of the 0–1 km updraft governed primarily by thermodynamic forcing. Within the 0.3–1 km layer, aerosols increase thermal buoyancy through enhanced condensational heating. Near the surface (0–0.3 km), aerosols reduce thermal buoyancy; however, this reduction is more than compensated by an increase in acceleration due to buoyancy-induced VPPGF, resulting in a net increase in vertical acceleration. This dynamical adjustment reflects the pressure response required to maintain balance in buoyancy-driven ascent and underscores the coupled thermodynamic–dynamic nature of the aerosol influence.

In addition to enhancing condensational heating, aerosols suppress low-level evaporative cooling by reorganizing the spatial relationship between updraft cores and precipitating regions. The low-level updraft becomes more concentrated and is displaced away from areas of intense rain evaporation and cold-pool formation. This spatial separation weakens the negative feedback associated with cold pools, allowing the convective system to remain more intense and organized. The combined effect is a warmer, more buoyant inflow region, a stronger and more persistent low-level updraft, enhanced convergence, and increased storm-relative inflow and helicity. These processes collectively render the environment more favorable for tornadogenesis, as summarized schematically in Fig. 11.

Recent theoretical studies (Grabowski and Morrison, 2020; Varble et al., 2023) suggest that warm-phase aerosol invigoration is constrained by the thermodynamic and dynamical conditions that control supersaturation near cloud base. In quasi-equilibrium regimes, condensation rates are largely determined by updraft velocity, limiting the direct impact of increased CCN concentrations. Within this framework, substantial warm-phase aerosol effects are most likely when aerosols modify the low-level conditions that set the initial updraft, particularly near cloud base where quasi-equilibrium assumptions may not strictly apply. Consistent with this perspective, our results demonstrate that aerosols can substantially influence low-level buoyancy and pressure-gradient forces, accelerating the 0–1 km updraft prior to parcels reaching quasi-equilibrium supersaturation. Moreover, in contrast to studies emphasizing nonlinear cold-pool lifting mechanisms, this case highlights a complementary pathway in which aerosol effects are exerted primarily through low-level thermodynamic enhancement and associated dynamical adjustments.

https://doi.org/10.5194/egusphere-2026-1730
Preprint. Discussion started: 4 May 2026

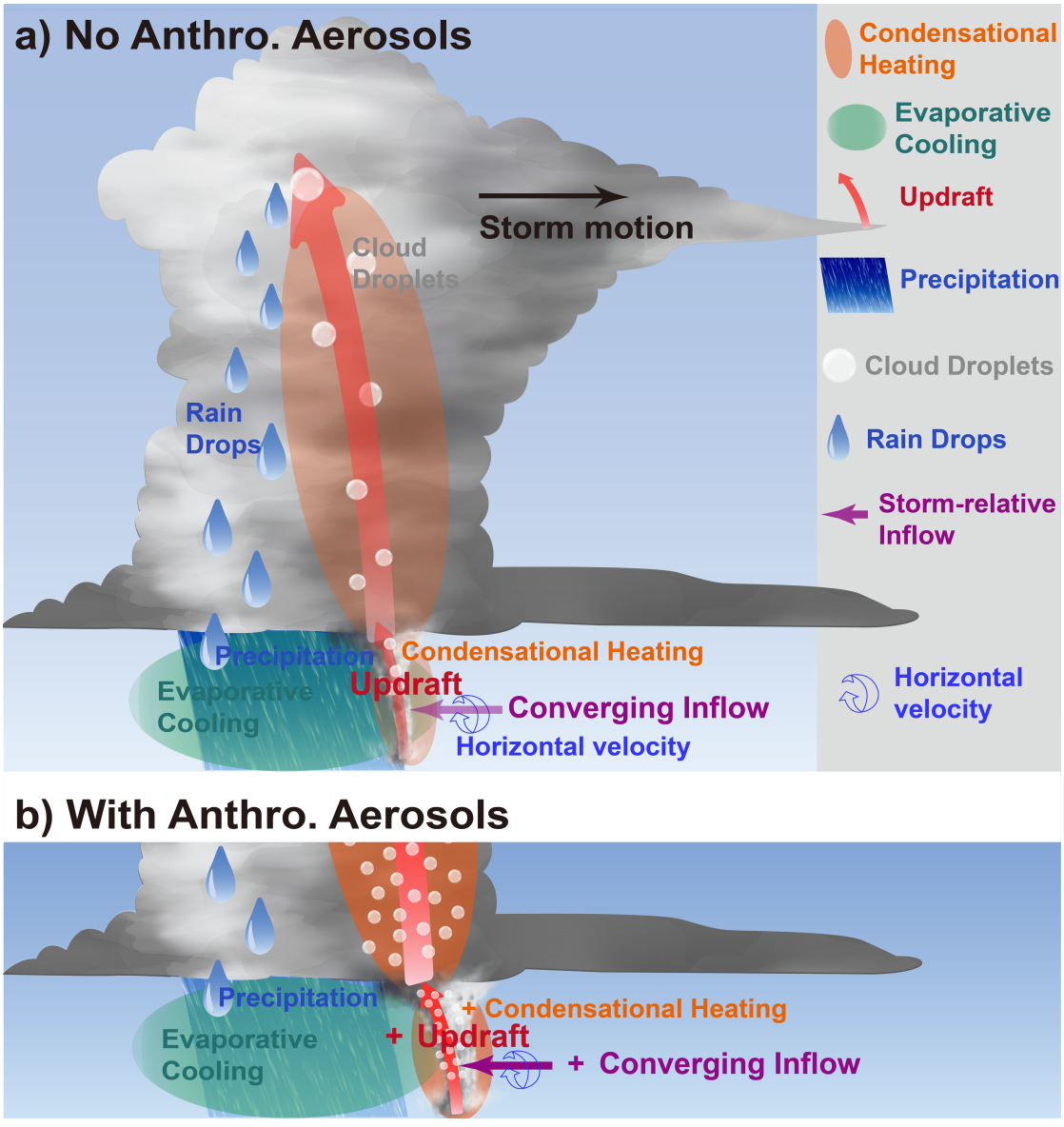

Figure 11. Schematic illustration of the aerosol effects on tornado potential, showing the case (a) without anthropogenic aerosols and (b) with anthropogenic aerosols. Below 1 km, aerosols (white particles) cause the 0–1 km updraft core (red arrows) to become more concentrated and to shift away from regions of strong rain evaporation (green shaded ovals). This spatial separation is associated with an aerosol-related enlargement of the spacing separating the updraft core from the primary precipitation area (blue shaded rhomboids). Consequently, aerosols intensify condensational latent heating (orange shaded ovals) and reduce near-surface rain-evaporation cooling, thereby increasing thermal buoyancy and vertical velocity. The strengthened buoyant updraft enhances low-level convergence and storm-relative inflow (purple arrows) below 1 km, allowing more horizontal vorticity (blue curved arrows) to be entrained into the storm and thereby increasing storm-relative helicity in the 0–1 km layer (SRH1). Overall, anthropogenic aerosols modify the low-level environment and help sustain storm dynamics, thereby enhancing tornado potential.

https://doi.org/10.5194/egusphere-2026-1730
Preprint. Discussion started: 4 May 2026

4 Conclusions

While aerosols are known to affect multiple atmospheric processes, especially clouds, precipitation, storms and lightning (e.g. Li et al., 2017; Li et al., 2019b), few studies have examined tornadoes. Here, we quantify how anthropogenic aerosols affect tornado potential for an EF3 supercell tornado. A data-assimilative WRF-Chem framework incorporating hybrid ETKF–3DVAR assimilation is employed to simulate the mesoscale organization of the storm, rainfall development and cold-pool features with reasonable fidelity, rendering a robust foundation for attributing changes in tornado-favorable environments to aerosol perturbations.

Overall, this study identifies a thermodynamically driven dynamical mechanism by which anthropogenic aerosols modify microphysical heating and buoyancy, leading to strengthened low-level updrafts, enhanced inflow, and increased storm-relative helicity. The new mechanism points to a new pathway toward the aerosol condensational invigoration effect by modulating low-level dynamic and thermodynamic conditions in a tornadic environment. These findings suggest that aerosol loading may be an important, yet underappreciated, factor in assessing tornado-favorable environments in polluted and rapidly urbanizing regions such as the Yangtze River Delta.

At the same time, it is admitted that the findings may not be generally valid as they are drawn from simulations of a single case using parameterized microphysics and a specific thermodynamic and dynamical configuration. Aerosol impacts may differ not only in strength but also in direction under different environmental conditions, aerosol regimes, and microphysical representations. Studying more cases is warranted with more advanced parameterizations of microphysics and observations of supersaturation, condensate loading acceleration, and cold-pool structure. The question of whether aerosols can materially alter the occurrence of tornadoes is also worthy of future investigation via occurrence-oriented tornado diagnostics (Zhang et al., 2025).

Appendix A: Validation of aerosol effects on STP

Following the original STP formulation (Thompson et al., 2003; Eq. 1 in the main text), several later formulas have been developed to improve its performance across broader convective regimes (Thompson et al., 2012) and for Chinese tornadic environments (Zhang et al., 2025). The normalization constants in the formulas were modified accordingly. To assess the robustness of our results in the aerosol effect on STP, we investigate these alternative STP formulas.

Thompson et al. (2012) described STP by variables in the effective inflow layer ($\mathrm{STP_{eff}}$, Eq. A1):

$$\mathrm{STP_{eff}} = \frac{\mathrm{ESRH}}{150\ \mathrm{m^2\ s^{-2}}} \cdot \frac{\mathrm{EBWD}}{20\ \mathrm{m\ s^{-1}}} \cdot \frac{2000 - \mathrm{MLLCL}}{1000\ \mathrm{m}} \cdot \frac{\mathrm{MLCAPE}}{1500\ \mathrm{J\ kg^{-1}}} \cdot \frac{200 + \mathrm{MLCIN}}{150\ \mathrm{J\ kg^{-1}}} \tag{A1}$$

The effective inflow layer begins at the lowest lifted-parcel level at which CAPE reaches at least 100 $\mathrm{J\ kg^{-1}}$ and CIN exceeds $-250\ \mathrm{J\ kg^{-1}}$, and its upper boundary is the highest contiguous parcel level that meets the same criteria. Accordingly, the effective storm relative helicity (ESRH) is integrated over this layer. The EBWD term is limited to 1.5 when EBWD exceeds 30 $\mathrm{m\ s^{-1}}$ and is assigned zero when EBWD is less than 12.5 $\mathrm{m\ s^{-1}}$. The MLLCL and MLCIN terms are assigned

https://doi.org/10.5194/egusphere-2026-1730
Preprint. Discussion started: 4 May 2026

a value of 1 when MLLCL is less than 1000 m and MLCIN exceeds -50 J kg^{-1}, respectively, and are assigned zero when MLLCL exceeds 2000 m and MLCIN is less than -200 J kg^{-1}, respectively.

Using a long-term sample of Chinese supercells, Zhang et al. (2025) revealed that 0–300 m kinematic parameters have a greater skill than those in the 0–1 km layer for separating tornadic from non-tornadic supercells. The calibrated STP parameter ($\mathrm{STP}_{\mathrm{300cn}}$) was proposed as:

$$\mathrm{STP}_{\mathrm{300cn}} = \frac{\mathrm{SRH300}}{12\ \mathrm{m^2\ s^{-2}}} \cdot \frac{\mathrm{SHR300}}{1.9\ \mathrm{m\ s^{-1}}} \cdot \frac{1600 - \mathrm{MULCL}}{600\ \mathrm{m}} \cdot \frac{\mathrm{MUCAPE}}{2000\ \mathrm{J\ kg^{-1}}} \cdot \frac{200 + \mathrm{MUCIN}}{150\ \mathrm{J\ kg^{-1}}} \tag{A2}$$

This formulation replaces 0–1 km AGL SRH1 and SHR6 terms in Eq. 1 with 0–300 m AGL storm-relative helicity (SRH300) and vector wind shear (SHR300), respectively, and adopts most-unstable-parcel CAPE, LCL, and CIN (MUCAPE, MULCL, and MUCIN, respectively). The SHR300 term is limited to 1.5 when SHR300 exceeds 2.85 m s^{-1}, and the MULCL and MUCIN terms are assigned a value of 1 when MULCL is less than 1000 m and MUCIN exceeds -50 J kg^{-1}, respectively, and are assigned a value of zero when MULCL exceeds 1600 m and MUCIN is less than -150 J kg^{-1}, respectively.

However, $\mathrm{STP}_{\mathrm{300cn}}$ was optimized primarily for occurrence discrimination in China, and its relevance to tornado intensity has not yet been validated. Since our focus is the aerosol effect on the intensity of an EF3 tornado, whose occurrence is not likely changed by aerosol abundance, we only use $\mathrm{STP}_{\mathrm{eff}}$ as the alternative formula to assess the robustness of our result. The $\mathrm{STP}_{\mathrm{eff}}$ area was tracked using the same method as described in Section 2.4.

Fig. A1 shows the time evolutions of $\mathrm{STP}_{\mathrm{eff}}$ and its component terms averaged over the tracked $\mathrm{STP}_{\mathrm{eff}}$ area. In both All and NoAero experiments, $\mathrm{STP}_{\mathrm{eff}}$ values exceed 1 but decrease sharply after 18:00 LST. Therefore they do not indicate a progressively more favorable environment at the time of tornado occurrence (19:00 LST). This disagreement with reality may stem from the lower discriminatory skill of $\mathrm{STP}_{\mathrm{eff}}$ than STP across different environmental regimes and convective modes (Brown et al., 2021; Zhang et al., 2025). Thus, it is less suitable than STP as the metric for further analysis. Nevertheless, $\mathrm{STP}_{\mathrm{eff}}$ still shows an aerosol-induced enhancement with the largest contribution from increases in the effective SRH (ESRH) term, thereby supporting the robustness of our results.

https://doi.org/10.5194/egusphere-2026-1730
Preprint. Discussion started: 4 May 2026

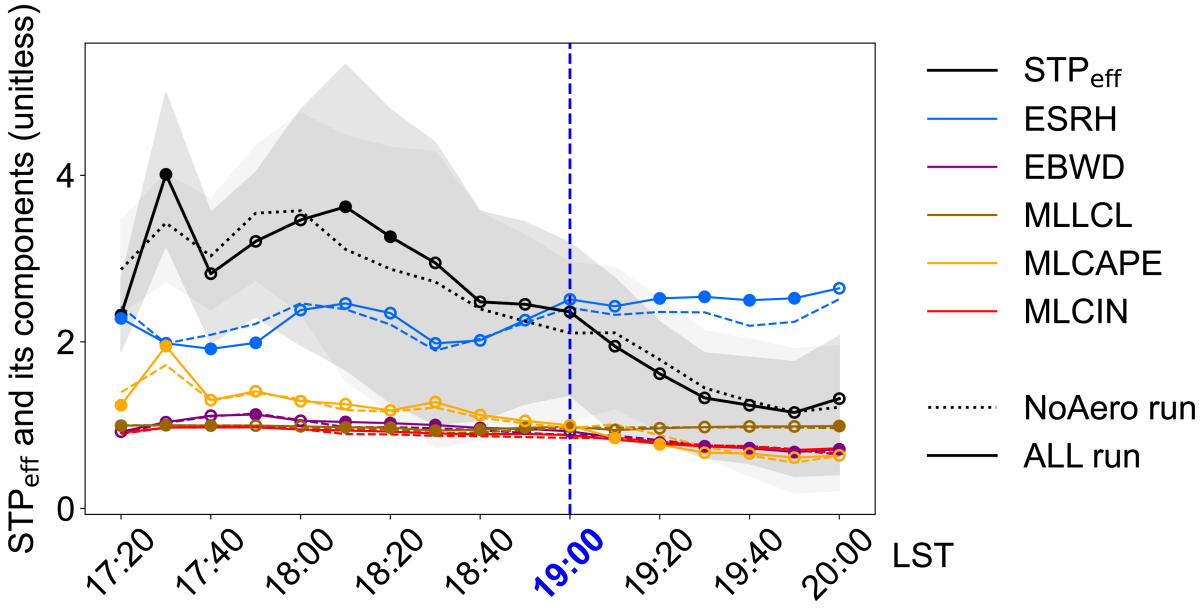

Figure A1. Same as Fig. 5 in the main text, but for the time evolution of $\mathrm{STP_{eff}}$ and its components (unitless) averaged over the tracked $\mathrm{STP_{eff}}$ area. The colored lines denote the ESRH term (sky blue), EBWD term (purple), MLLCL term (brown), MLCAPE term (orange), and MLCIN term (red).

Code availability. WRF-Chem (WRF v4.2.2) is distributed as part of the WRF modeling system and is accessible through the official GitHub site (https://github.com/wrf-model/WRF). WRFlux v1.2.0 is available on GitHub and has a Zenodo record (https://zenodo.org/records/4664425; DOI: https://doi.org/10.5281/zenodo.4664425). The meic2wrf processor is available on gitee (https://gitee.com/jinfan0931/meic2wrf). The bio_emiss processor can be obtained from the NSF NCAR Atmospheric Chemistry Observations & Modeling (ACOM) "Download WRF-Chem Processors" page (https://www.acom.ucar.edu/wrf-chem/download.shtml).

Data availability. The NCEP FNL Operational Global Analysis ($1^\circ \times 1^\circ$, 6-hourly) used for initial fields and lateral meteorological boundary conditions is available through NSF National Center for Atmospheric Research (NCAR) Geoscience Data Exchange (GDEX) (https://gdex.ucar.edu/datasets/d083002/; DOI: https://doi.org/10.5065/D6M043C6). The GLC_FCS30-2020 land-cover dataset (version 1.2), provided by the Aerospace Information Research Institute, Chinese Academy of Sciences, is available via CASEarth Data (https://zenodo.org/records/4280923). MODIS NDVI was obtained from the Terra MOD13Q1 Version 6.1 16-day 250 m vegetation index dataset (https://www.earthdata.nasa.gov/data/catalog/lpcloud-mod13q1-061; DOI: https://doi.org/10.5067/MODIS/MOD13Q1.061). Anthropogenic emissions were derived from the Tsinghua MEIC inventory (http://meicmodel.org.cn/). The MEGAN default input dataset is available from the UCI BAI MEGAN portal (https://bai.ess.uci.edu/megan), and has a Zenodo record (https://zenodo.org/records/10521585; DOI: https://doi.org/10.5281/zenodo.10521585). The CESM2.2 CAM-Chem global fields used for chemical lateral boundary conditions are avail-

https://doi.org/10.5194/egusphere-2026-1730
Preprint. Discussion started: 4 May 2026

able from NSF NCAR GDEX (https://gdex.ucar.edu/datasets/d313008/; DOI: https://doi.org/10.5065/XS0R-QE86). The single-polarization Doppler radar data and surface AWS observations were obtained from a meteorological agency and cannot be redistributed by the authors due to data-use restrictions. The derived products generated in this study and the scripts can be shared by the corresponding author upon reasonable request.

Author contributions. RW and TF conceptualized the study. RW performed the simulations and analyses and drafted the manuscript. TF and ZL supervised the work, contributed to the scientific discussion, provided computational resources, and revised the manuscript. JG provided the observational datasets for data assimilation and contributed to the conceptualization and scientific discussions. All authors approved the final manuscript.

Competing interests. One of the authors is a member of the editorial board of Atmospheric Chemistry and Physics. The authors declare that they have no other competing interests.

Acknowledgements. We thank Yuejian Zhu (CMA Earth System Modeling and Prediction Centre) for guidance on the data-assimilation configuration. We thank Yuan Jiang and Ruichun Wang (CMA Earth System Modeling and Prediction Centre) for guidance on quality control of radar and surface-station observations, respectively, and Tianmeng Chen (State Key Laboratory of Severe Weather Meteorological Science and Technology & the Specialized Meteorological Support Technology Research Center, Chinese Academy of Meteorological Sciences) for guidance on observational data processing.

Financial support. This research has been supported by the National Natural Science Foundation of China (grant nos. 42030606, 42230601 and 42375073).

https://doi.org/10.5194/egusphere-2026-1730
Preprint. Discussion started: 4 May 2026

References

Abulikemu, A., Xu, X., Wang, Y., Ding, J., Zhang, S., and Shen, W.: A modeling study of convection initiation prior to the merger of a sea-breeze front and a gust front, Atmos. Res., 182, 10–19, https://doi.org/10.1016/j.atmosres.2016.07.003, 2016.

Abulikemu, A., Wang, Y., Gao, R., Wang, Y., and Xu, X.: A numerical study of convection initiation associated with a gust front in Bohai Bay region, North China, J. Geophys. Res.-Atmos., 124, 13 843–13 860, https://doi.org/10.1029/2019JD030883, 2019.

Adams, R. and Bischof, L.: Seeded region growing, IEEE Trans. Pattern Anal. Mach. Intell., 16, 641–647, https://doi.org/10.1109/34.295913, 1994.

Andreae, M. O., Rosenfeld, D., Artaxo, P., Costa, A. A., Frank, G. P., Longo, K. M., and Silva-Dias, M. A. F.: Smoking rain clouds over the Amazon, Science, 303, 1337–1342, https://doi.org/10.1126/science.1092779, 2004.

Barrett, B. S. and Gensini, V. A.: Variability of central United States April-May tornado day likelihood by phase of the Madden–Julian Oscillation, Geophys. Res. Lett., 40, 2790–2795, https://doi.org/10.1002/grl.50522, 2013.

Berenguer, M., Sempere-Torres, D., Corral, C., and Sánchez-Diezma, R.: A fuzzy logic technique for identifying nonprecipitating echoes in radar scans, J. Atmos. Oceanic Technol., 23, 1157–1180, https://doi.org/10.1175/JTECH1914.1, 2006.

Brotzge, J. A., Nelson, S. E., Thompson, R. L., and Smith, B. T.: Tornado probability of detection and lead time as a function of convective mode and environmental parameters, Wea. Forecasting, 28, 1261–1276, https://doi.org/10.1175/WAF-D-12-00119.1, 2013.

Brown, M. C., Nowotarski, C. J., Dean, A. R., Smith, B. T., Thompson, R. L., and Peters, J. M.: The Early Evening Transition in Southeastern U.S. Tornado Environments, Wea. Forecasting, 36, 1431–1452, https://doi.org/10.1175/WAF-D-20-0191.1, 2021.

Buehner, M.: Ensemble-derived stationary and flow-dependent background-error covariances: Evaluation in a quasi-operational NWP setting, Q. J. R. Meteorol. Soc., 131, 1013–1043, https://doi.org/10.1256/qj.04.15, 2005.

Cao, Q., Jiang, B., Shen, X., Lin, W., and Chen, J.: Microphysics effects of anthropogenic aerosols on urban heavy precipitation over the Pearl River Delta, China, Atmos. Res., 253, 105 478, https://doi.org/10.1016/j.atmosres.2021.105478, 2021.

Chapman, E. G., Gustafson, W. I., Easter, R. C., Barnard, J. C., Ghan, S. J., Pekour, M. S., and Fast, J. D.: Coupling aerosol-cloud-radiative processes in the WRF-Chem model: Investigating the radiative impact of elevated point sources, Atmos. Chem. Phys., 9, 945–964, https://doi.org/10.5194/acp-9-945-2009, 2009.

Chen, Q., Fan, J., Yin, Y., and Han, B.: Aerosol impacts on mesoscale convective systems forming under different vertical wind shear conditions, J. Geophys. Res.-Atmos., 125, e2018JD030 027, https://doi.org/10.1029/2018JD030027, 2020.

China Meteorological Administration: Quality control of meteorological observation data – Surface (Standard No. QX/T 118-2020), https://www.cma.gov.cn/zfxxgk/gknr/flfgbz/bz/202209/P020220921713136385056.pdf, last access: 20 February 2026, 2020.

Coffer, B. E., Parker, M. D., Thompson, R. L., Smith, B. T., and Jewell, R. E.: Using near-ground storm-relative helicity in supercell tornado forecasting, Wea. Forecasting, 34, 1417–1435, https://doi.org/10.1175/WAF-D-19-0115.1, 2019.

Coffer, B. E., Taszarek, M., and Parker, M. D.: Near-ground wind profiles of tornadic and nontornadic environments in the United States and Europe from ERA5 reanalyses, Wea. Forecasting, 35, 2621–2638, https://doi.org/10.1175/WAF-D-20-0153.1, 2020.

Coffer, B. E., Parker, M. D., Peters, J. M., and Wade, A. R.: Supercell low-level mesocyclones: Origins of inflow and vorticity, Mon. Wea. Rev., 151, 2205–2232, https://doi.org/10.1175/MWR-D-22-0269.1, 2023.

Craven, J. P. and Brooks, H. E.: Baseline climatology of sounding-derived parameters associated with deep, moist convection, Natl. Weather Dig., 28, 13–24, 2004.

https://doi.org/10.5194/egusphere-2026-1730
Preprint. Discussion started: 4 May 2026

Dahl, J. M. L., Parker, M. D., and Wicker, L. J.: Imported and storm-generated near-ground vertical vorticity in a simulated supercell, J. Atmos. Sci., 71, 3027–3051, https://doi.org/10.1175/JAS-D-13-0123.1, 2014.

Davies-Jones, R.: Streamwise vorticity: The origin of updraft rotation in supercell storms, J. Atmos. Sci., 41, 2991–3006, https://doi.org/10.1175/1520-0469(1984)041<2991:SVTOOU>2.0.CO;2, 1984.

Evensen, G.: Sequential data assimilation with a nonlinear quasi-geostrophic model using Monte Carlo methods to forecast error statistics, J. Geophys. Res.-Oceans, 99, 10 143–10 162, https://doi.org/10.1029/94JC00572, 1994.

Fan, J. and Khain, A.: Comments on "Do ultrafine cloud condensation nuclei invigorate deep convection?", J. Atmos. Sci., 78, 329–339, https://doi.org/10.1175/JAS-D-20-0218.1, 2021.

Fan, J., Zhang, R., Li, G., and Tao, W.-K.: Effects of aerosols and relative humidity on cumulus clouds, J. Geophys. Res.-Atmos., 112, D14 204, https://doi.org/10.1029/2006JD008136, 2007.

Fan, J., Rosenfeld, D., Zhang, Y., Giangrande, S. E., Li, Z., Machado, L. A. T., Martin, S. T., Yang, Y., Wang, J., Artaxo, P., Barbosa, H. M. J., Braga, R. C., Comstock, J. M., Feng, Z., Gao, W., Gomes, H. B., Mei, F., Pöhlker, C., Pöhlker, M. L., Pöschl, U., and de Souza, R. A. F.: Substantial convection and precipitation enhancements by ultrafine aerosol particles, Science, 359, 411–418, https://doi.org/10.1126/science.aan8461, 2018.

Fan, J., Wang, J., and Lin, Y.: Urbanization may enhance tornado potential: A single case report, Front. Earth Sci., 11, 1148 506, https://doi.org/10.3389/feart.2023.1148506, 2023.

Fan, J., Zhang, Y., Li, Z., Yan, H., Prabhakaran, T., Rosenfeld, D., and Khain, A.: Unveiling aerosol impacts on deep convective clouds: Scientific concept, modeling, observational analysis, and future direction, J. Geophys. Res.-Atmos., 130, e2024JD041 931, https://doi.org/10.1029/2024JD041931, 2025.

Feng, T., Yuan, T., Cao, J., Wang, Z., Zhi, R., Hu, Z., and Huang, J.: The influence of dust on extreme precipitation at a large city in North China, Sci. Total Environ., 901, 165 890, https://doi.org/10.1016/j.scitotenv.2023.165890, 2023.

Fischer, J. and Dahl, J. M. L.: The relative importance of updraft and cold pool characteristics in supercell tornadogenesis using highly idealized simulations, J. Atmos. Sci., 77, 4089–4107, https://doi.org/10.1175/JAS-D-20-0126.1, 2020.

Fischer, J., Dahl, J. M. L., Coffer, B. E., Houser, J. L., Markowski, P. M., Parker, M. D., Weiss, C. C., and Schueth, A.: Supercell tornadogenesis: Recent progress in our state of understanding, Bull. Amer. Meteor. Soc., 105, E1084–E1097, https://doi.org/10.1175/BAMS-D-23-0031.1, 2024.

Frazier, A. E., Hemingway, B. L., and Brasher, J. P.: Land surface heterogeneity and tornado occurrence: an analysis of Tornado Alley and Dixie Alley, Geomat. Nat. Hazards Risk, 10, 1475–1492, https://doi.org/10.1080/19475705.2019.1583292, 2019.

Göbel, M.: WRFlux: v1.2 (v1.2.0), Zenodo [code], https://doi.org/10.5281/zenodo.4664425, 2021.

Goldacker, N. A. and Parker, M. D.: Assessing the comparative effects of storm-relative helicity components within right-moving supercell environments, J. Atmos. Sci., 80, 2805–2822, https://doi.org/10.1175/JAS-D-22-0253.1, 2023.

Grabowski, W. W.: Can the impact of aerosols on deep convection be isolated from meteorological effects in atmospheric observations?, J. Atmos. Sci., 75, 3347–3363, https://doi.org/10.1175/JAS-D-18-0105.1, 2018.

Grabowski, W. W. and Morrison, H.: Do ultrafine cloud condensation nuclei invigorate deep convection?, J. Atmos. Sci., 77, 2567–2583, https://doi.org/10.1175/JAS-D-20-0012.1, 2020.

Grams, J. S., Thompson, R. L., Snively, D. V., Prentice, J. A., Hodges, G. M., and Reames, L. J.: A climatology and comparison of parameters for significant tornado events in the United States, Wea. Forecasting, 27, 106–123, https://doi.org/10.1175/WAF-D-11-00008.1, 2012.

https://doi.org/10.5194/egusphere-2026-1730
Preprint. Discussion started: 4 May 2026

Grell, G. A., Peckham, S. E., Schmitz, R., McKeen, S. A., Frost, G., Skamarock, W. C., and Eder, B.: Fully coupled "online" chemistry within the WRF model, Atmos. Environ., 39, 6957–6975, https://doi.org/10.1016/j.atmosenv.2005.04.027, 2005.

Grzych, M. L., Lee, B. D., and Finley, C. A.: Thermodynamic analysis of supercell rear-flank downdrafts from Project ANSWERS, Mon. Wea. Rev., 135, 240–246, https://doi.org/10.1175/MWR3288.1, 2007.

Guarriello, F., Nowotarski, C. J., and Epifanio, C. C.: Effects of the low-level wind profile on outflow position and near-surface vertical vorticity in simulated supercell thunderstorms, J. Atmos. Sci., 75, 731–753, https://doi.org/10.1175/JAS-D-17-0174.1, 2018.

Hohenegger, C. and Schär, C.: Predictability and error growth dynamics in cloud-resolving models, J. Atmos. Sci., 64, 4467–4478, https://doi.org/10.1175/2007JAS2143.1, 2007.

Igel, A. L. and van den Heever, S. C.: Invigoration or enervation of convective clouds by aerosols?, Geophys. Res. Lett., 48, e2021GL093 804, https://doi.org/10.1029/2021GL093804, 2021.

Jeevanjee, N. and Romps, D. M.: Effective buoyancy, inertial pressure, and the mechanical generation of boundary-layer mass flux by cold pools, J. Atmos. Sci., 72, 3199–3213, https://doi.org/10.1175/JAS-D-14-0349.1, 2015.

Jiang, J. H., Su, H., Huang, L., Wang, Y., Massie, S., Zhao, B., Omar, A., and Wang, Z.: Contrasting effects on deep convective clouds by different types of aerosols, Nat. Commun., 9, 3874, https://doi.org/10.1038/s41467-018-06280-4, 2018.

Kalina, E. A., Friedrich, K., Morrison, H., and Bryan, G. H.: Aerosol effects on idealized supercell thunderstorms in different environments, J. Atmos. Sci., 71, 4558–4580, https://doi.org/10.1175/JAS-D-14-0037.1, 2014.

Kawecki, S., Henebry, G. M., and Steiner, A. L.: Effects of urban plume aerosols on a mesoscale convective system, J. Atmos. Sci., 73, 4641–4660, https://doi.org/10.1175/JAS-D-16-0084.1, 2016.

Kellner, O. and Niyogi, D.: Land surface heterogeneity signature in tornado climatology? an illustrative analysis over Indiana, 1950–2012, Earth Interact., 18, 1–32, https://doi.org/10.1175/2013EI000548.1, 2014.

Khain, A., Rosenfeld, D., and Pokrovsky, A.: Aerosol impact on the dynamics and microphysics of deep convective clouds, Q. J. R. Meteorol. Soc., 131, 2639–2663, https://doi.org/10.1256/qj.04.62, 2005.

Kong, X., Chen, G., Bai, L., Ran, L., Zhang, S., and Meng, Z.: A mesoscale-to-LES modeling of tornado-like vortex and associated local strong winds in urban area, J. Geophys. Res.-Atmos., 130, e2025JD044 574, https://doi.org/10.1029/2025JD044574, 2025.

LeBel, L. J., Tang, B. H., and Lazear, R. A.: Examining terrain effects on an Upstate New York tornado event utilizing a high-resolution model simulation, Wea. Forecasting, 36, 2001–2020, https://doi.org/10.1175/WAF-D-21-0018.1, 2021.

Lebo, Z. J. and Morrison, H.: Dynamical effects of aerosol perturbations on simulated idealized squall lines, Mon. Wea. Rev., 142, 991–1009, https://doi.org/10.1175/MWR-D-13-00156.1, 2014.

Lepore, C., Tippett, M. K., and Allen, J. T.: ENSO-based probabilistic forecasts of March–May U.S. tornado and hail activity, Geophys. Res. Lett., 44, 9093–9101, https://doi.org/10.1002/2017GL074781, 2017.

Lerach, D. G. and Cotton, W. R.: Comparing aerosol and low-level moisture influences on supercell tornadogenesis: Three-dimensional idealized simulations, J. Atmos. Sci., 69, 969–987, https://doi.org/10.1175/JAS-D-11-043.1, 2012.

Lerach, D. G., Gaudet, B. J., and Cotton, W. R.: Idealized simulations of aerosol influences on tornadogenesis, Geophys. Res. Lett., 35, 2008GL035 617, https://doi.org/10.1029/2008GL035617, 2008.

Li, F., Chavas, D. R., Medeiros, B., Reed, K. A., and Rasmussen, K. L.: Upstream surface roughness and terrain are strong drivers of contrast in tornado potential between North and South America, P. Natl. Acad. Sci. USA, 121, e2315425 121, https://doi.org/10.1073/pnas.2315425121, 2024.

https://doi.org/10.5194/egusphere-2026-1730
Preprint. Discussion started: 4 May 2026

Li, J., Ping, F., Zhou, S., and Shen, X.: Numerical simulation of a strong tornado in eastern China with different microphysical schemes, Atmos. Sci. Lett., 20, e875, https://doi.org/10.1002/asl.875, 2019a.

Li, Z., Niu, F., Fan, J., Liu, Y., Rosenfeld, D., and Ding, Y.: Long-term impacts of aerosols on the vertical development of clouds and precipitation, Nat. Geosci., 4, 888–894, https://doi.org/10.1038/ngeo1313, 2011.

Li, Z., Rosenfeld, D., and Fan, J.: Aerosols and their impact on radiation, clouds, precipitation, and severe weather events, Oxford Research Encyclopedias: Environmental Science, Oxford University Press, https://doi.org/10.1093/acrefore/9780199389414.013.126, oxford Research Encyclopedia of Environmental Science, accessed: 10 Feb 2026, 2017.

Li, Z., Wang, Y., Guo, J., Zhao, C., Cribb, M. C., Dong, X., Fan, J., Gong, D., Huang, J., Jiang, M., Jiang, Y., Lee, S. S., Li, H., Li, J., Liu, J., Qian, Y., Rosenfeld, D., Shan, S., Sun, Y., Wang, H., Xin, J., Yan, X., Yang, X., Yang, X.-Q., Zhang, F., and Zheng, Y.: East Asian Study of Tropospheric Aerosols and their Impact on Regional Clouds, Precipitation, and Climate (EAST-AIRCPC), J. Geophys. Res.-Atmos., 124, 13 026–13 054, https://doi.org/10.1029/2019JD030758, 2019b.

Litta, A. J., Mohanty, U. C., Kiran Prasad, S., Mohapatra, M., Tyagi, A., and Sahu, S. C.: Simulation of tornado over Orissa (India) on March 31, 2009, using WRF–NMM model, Nat. Hazards, 61, 1219–1242, https://doi.org/10.1007/s11069-011-9979-1, 2012.

Maddox, R. A.: An evaluation of tornado proximity wind and stability data, Mon. Wea. Rev., 104, 133–142, https://doi.org/10.1175/1520-0493(1976)104<0133:AEOTPW>2.0.CO;2, 1976.

Marinescu, P. J., van den Heever, S. C., Heikenfeld, M., Barrett, A. I., Barthlott, C., Hoose, C., Fan, J., Fridlind, A. M., Matsui, T., Miltenberger, A. K., Stier, P., Vie, B., White, B. A., and Zhang, Y.: Impacts of varying concentrations of cloud condensation nuclei on deep convective cloud updrafts – a multimodel assessment, J. Atmos. Sci., 78, 1147–1172, https://doi.org/10.1175/JAS-D-20-0200.1, 2021.

Markert, A., Griffin, R., Knupp, K., Molthan, A., and Coleman, T.: A spatial pattern analysis of land surface roughness heterogeneity and its relationship to the initiation of weak tornadoes, Earth Interact., 23, 1–28, https://doi.org/10.1175/EI-D-18-0010.1, 2019.

Markowski, P. M. and Richardson, Y. P.: The influence of environmental low-level shear and cold pools on tornadogenesis: Insights from idealized simulations, J. Atmos. Sci., 71, 243–275, https://doi.org/10.1175/JAS-D-13-0159.1, 2014.

Markowski, P. M., Straka, J. M., and Rasmussen, E. N.: Direct surface thermodynamic observations within the rear-flank downdrafts of nontornadic and tornadic supercells, Mon. Wea. Rev., 130, 1692–1721, https://doi.org/10.1175/1520-0493(2002)130<1692:DSTOWT>2.0.CO;2, 2002.

National Weather Service: Weather fatalities, injuries, and damage statistics: 80-year summary, National Weather Service (NWS) online report, https://www.weather.gov/media/hazstat/80year_2024.pdf, last access: 20 February 2026, 2024.

Öktem, R., Romps, D. M., and Varble, A. C.: No warm-phase invigoration of convection detected during GoAmazon, J. Atmos. Sci., 80, 2345–2364, https://doi.org/10.1175/JAS-D-22-0241.1, 2023.

Orf, L., Wilhelmson, R., Lee, B., Finley, C., and Houston, A.: Evolution of a long-track violent tornado within a simulated supercell, Bull. Amer. Meteorol. Soc., 98, 45–68, https://doi.org/10.1175/BAMS-D-15-00073.1, 2017.

Peters, J. M., Coffer, B. E., Parker, M. D., Nowotarski, C. J., Mulholland, J. P., Nixon, C. J., and Allen, J. T.: Disentangling the influences of storm-relative flow and horizontal streamwise vorticity on low-level mesocyclones in supercells, J. Atmos. Sci., 80, 129–149, https://doi.org/10.1175/JAS-D-22-0114.1, 2023.

Radhakrishna, B., Fabry, F., and Kilambi, A.: Fuzzy logic algorithms to identify birds, precipitation, and ground clutter in S-band radar data using polarimetric and nonpolarimetric variables, J. Atmos. Oceanic Technol., 36, 2401–2414, https://doi.org/10.1175/JTECH-D-19-0088.1, 2019.

https://doi.org/10.5194/egusphere-2026-1730
Preprint. Discussion started: 4 May 2026

Romps, D. M., Latimer, K., Zhu, Q., Jurkat-Witschas, T., Mahnke, C., Prabhakaran, T., Weigel, R., and Wendisch, M.: Air pollution unable to intensify storms via warm-phase invigoration, Geophys. Res. Lett., 50, e2022GL100 409, https://doi.org/10.1029/2022GL100409, 2023.

Rosenfeld, D., Lohmann, U., Raga, G. B., O'Dowd, C. D., Kulmala, M., Fuzzi, S., Reissell, A., and Andreae, M. O.: Flood or drought: how do aerosols affect precipitation?, Science, 321, 1309–1313, https://doi.org/10.1126/science.1160606, 2008.

Saide, P. E., Spak, S. N., Pierce, R. B., Otkin, J. A., Schaack, T. K., Heidinger, A. K., da Silva, A. M., Kacenelenbogen, M., Redemann, J., and Carmichael, G. R.: Central American biomass burning smoke can increase tornado severity in the U.S., Geophys. Res. Lett., 42, 956–965, https://doi.org/10.1002/2014GL062826, 2015.

Saide, P. E., Thompson, G., Eidhammer, T., da Silva, A. M., Pierce, R. B., and Carmichael, G. R.: Assessment of biomass burning smoke influence on environmental conditions for multiyear tornado outbreaks by combining aerosol-aware microphysics and fire emission constraints, J. Geophys. Res.-Atmos., 121, 10 294–10 311, https://doi.org/10.1002/2016JD025056, 2016.

Sasaki, Y.: An objective analysis based on the variational method, J. Meteorol. Soc. Jpn., 36, 77–88, https://doi.org/10.2151/jmsj1923.36.3_77, 1958.

Shang, Y., Zhang, B., Qin, Z., and Li, X.: Independent quality control of high spatiotemporal resolution surface temperature observations from automatic stations (in Chinese), Plateau Meteorology, 43, 967–981, https://doi.org/10.7522/j.issn.1000-0534.2023.00105, 2024.

Snook, N., Xue, M., and Jung, Y.: Tornado-resolving ensemble and probabilistic predictions of the 20 May 2013 Newcastle–Moore EF5 tornado, Mon. Wea. Rev., 147, 1215–1235, https://doi.org/10.1175/MWR-D-18-0236.1, 2019.

Stevens, B. and Feingold, G.: Untangling aerosol effects on clouds and precipitation in a buffered system, Nature, 461, 607–613, https://doi.org/10.1038/nature08281, 2009.

Sun, T., Sun, J., Chen, Y., Zhang, Y., Ying, Z., and Chen, H.: Improving short-term precipitation forecasting with radar data assimilation and a multiscale hybrid ensemble–variational strategy, Mon. Wea. Rev., 150, 2357–2377, https://doi.org/10.1175/MWR-D-21-0325.1, 2022.

Sun, Z., Xue, M., Zhu, K., and Zhou, B.: Prediction of an EF4 supercell tornado in Funing, China: Resolution dependency of simulated tornadoes and their structures, Atmos. Res., 229, 175–189, https://doi.org/10.1016/j.atmosres.2019.06.019, 2019.

Tanamachi, R. L., Bluestein, H. B., Xue, M., Lee, W., Orzel, K. A., Frasier, S. J., and Wakimoto, R. M.: Near-surface vortex structure in a tornado and in a sub-tornado-strength convective-storm vortex observed by a mobile, W-band radar during VORTEX2, Mon. Wea. Rev., 141, 3661–3690, https://doi.org/10.1175/MWR-D-12-00331.1, 2013.

Taszarek, M., Czernecki, B., Walczakiewicz, S., Mazur, A., and Kolendowicz, L.: An isolated tornadic supercell of 14 July 2012 in Poland – a prediction technique within the use of coarse-grid WRF simulation, Atmos. Res., 178-179, 367–379, https://doi.org/10.1016/j.atmosres.2016.04.009, 2016.

Thompson, R., Smith, B., Grams, J., Dean, A., and Broyles, C.: Convective modes for significant severe thunderstorms in the contiguous United States. Part II: supercell and QLCS tornado environments, Wea. Forecasting, 27, 1136–1154, https://doi.org/10.1175/WAF-D-11-00116.1, 2012.

Thompson, R. L., Edwards, R., Hart, J. A., Elmore, K. L., and Markowski, P.: Close proximity soundings within supercell environments obtained from the Rapid Update Cycle, Wea. Forecasting, 18, 1243–1261, https://doi.org/10.1175/1520-0434(2003)018<1243:CPSWSE>2.0.CO;2, 2003.

Tippett, M. K.: Robustness of relations between the MJO and U.S. tornado occurrence, Mon. Wea. Rev., 146, 3873–3884, https://doi.org/10.1175/MWR-D-18-0207.1, 2018.

Tippett, M. K., Lepore, C., and L'Heureux, M. L.: Predictability of a tornado environment index from El Niño–Southern Oscillation (ENSO) and the Arctic Oscillation, Weather Clim. Dynam., 3, 1063–1075, https://doi.org/10.5194/wcd-3-1063-2022, 2022.

https://doi.org/10.5194/egusphere-2026-1730
Preprint. Discussion started: 4 May 2026

Varble, A. C., Igel, A. L., Morrison, H., Grabowski, W. W., and Lebo, Z. J.: Opinion: A critical evaluation of the evidence for aerosol invigoration of deep convection, Atmos. Chem. Phys., 23, 13 791–13 808, https://doi.org/10.5194/acp-23-13791-2023, 2023.

Wang, C.: A modeling study of the response of tropical deep convection to the increase of cloud condensation nuclei concentration: 2. radiation and tropospheric chemistry, J. Geophys. Res.-Atmos., 110, D22 204, https://doi.org/10.1029/2005JD005829, 2005.

Wang, J., Zhang, H., Chen, J., Deng, G., and Xia, Y.: Construction of multiscale initial perturbations and the associated impacts on convection-permitting ensemble forecasting, Atmos. Res., 297, 107 121, https://doi.org/10.1016/j.atmosres.2023.107121, 2024.

Wang, X., Snyder, C., and Hamill, T. M.: On the theoretical equivalence of differently proposed ensemble–3DVAR hybrid analysis schemes, Mon. Wea. Rev., 135, 222–227, https://doi.org/10.1175/MWR3282.1, 2007.

World Meteorological Organization: Tornado intensity, International Cloud Atlas, https://cloudatlas.wmo.int/en/tornado-intensity.html, last access: 20 February 2026, 2017.

Wu, B., Wei, M., and Li, Y.: Dual-polarization radar observations of the evolution of a supercell tornado and analysis of the echo mechanisms, Atmosphere, 13, 797, https://doi.org/10.3390/atmos13050797, 2022.

Xiao, H., Yin, Y., Chen, Q., and Zhao, P.: Impact of aerosol and freezing level on orographic clouds: A sensitivity study, Atmos. Res., 176-177, 19–28, https://doi.org/10.1016/j.atmosres.2016.02.014, 2016.

Xue, M., Hu, M., and Schenkman, A. D.: Numerical prediction of the 8 May 2003 Oklahoma City tornadic supercell and embedded tornado using ARPS with the assimilation of WSR-88D data, Wea. Forecasting, 29, 39–62, https://doi.org/10.1175/WAF-D-13-00029.1, 2014.

Yang, S., Li, D., Duan, Y., Chen, Y., Liu, Z., and Huang, X.: Assimilating precipitation data via full-hydrometeor scheme in WRF 4D-Var for convective precipitation forecast associated with the Northeast China cold vortex (NCCV), J. Geophys. Res.-Atmos., 130, e2024JD042 427, https://doi.org/10.1029/2024JD042427, 2025.

Yuan, C., Bai, Y., Sun, P., Bai, H., and Xia, L.: Microphysical insights into a tornadic supercell from dual-polarization radar observations in Jiangsu, China on 14 May 2021, J. Meteorol. Res., 38, 303–320, https://doi.org/10.1007/s13351-024-3102-5, 2024.

Yun, Y., Zhang, D., Gao, W., Yin, J., Zhao, C., Li, J., Guo, J., and Liu, H.: Spatiotemporal variations of the effects of aerosols on clouds and precipitation in an extreme-rain-producing MCS in South China, J. Geophys. Res.-Atmos., 129, e2023JD040 014, https://doi.org/10.1029/2023JD040014, 2024.

Zhang, F., Snyder, C., and Rotunno, R.: Effects of moist convection on mesoscale predictability, J. Atmos. Sci., 60, 1173–1185, https://doi.org/10.1175/1520-0469(2003)060<1173:EOMCOM>2.0.CO;2, 2003.

Zhang, R., Xue, M., and Yu, X.: Environments of tornadic and non-tornadic supercells in China and optimized significant tornado parameter for China region, Q. J. R. Meteorol. Soc., 151, e5027, https://doi.org/10.1002/qj.5027, 2025.

Zheng, K. and Chen, B.: Sensitivities of tornadogenesis to drop size distribution in a simulated subtropical supercell over eastern China, Adv. Atmos. Sci., 31, 657–668, https://doi.org/10.1007/s00376-013-3143-7, 2014.

Zhuang, X., Min, J., Zhang, L., Wang, S., Wu, N., and Zhu, H.: Insights into convective-scale predictability in East China: Error growth dynamics and associated impact on precipitation of warm-season convective events, Adv. Atmos. Sci., 37, 893–911, https://doi.org/10.1007/s00376-020-9269-5, 2020.